



ASME Post-Print (After Review) Repository

Institutional Repository Cover Sheet

Ecole Polytechnique Fédérale de Lausanne, Switzerland
Infoscience (<https://infoscience.epfl.ch/>)
<https://infoscience.epfl.ch/record/282784>

Patrick Hubert

First

Wagner

Last

mail@patrick-wagner.net

E-mail

ASME Paper Title: Theoretical and Experimental Investigation of a 34 Watt Radial-Inflow Steam Turbine

with Partial-Admission

Authors: Patrick Hubert Wagner, Jan Van herle, Jürg Schiffmann

ASME Journal Title: Journal of Engineering for Gas Turbines and Power. Aug 2021, 143(8):

Paper No: GTP-20-1474, 081002 (14 pages)

Date of Publication (VOR* Online): March 31, 2021

ASME Digital Collection URL:

<https://asmedigitalcollection.asme.org/gasturbinespower/article-abstract/143/8/081002/1093945>

DOI: <https://doi.org/10.1115/1.4049483>

*VOR (version of record)

THEORETICAL AND EXPERIMENTAL INVESTIGATION OF A 34 WATT RADIAL-INFLOW STEAM TURBINE WITH PARTIAL-ADMISSION

Patrick H. Wagner

Laboratory for Applied Mechanical Design
Institute of Mechanical Engineering
École Polytechnique Fédérale de Lausanne
Neuchâtel, Neuchâtel, 2000
Switzerland
Email: mail@patrick-wagner.net

Jan Van herle

Group of Energy Materials
IGM
EPFL
Sion, Valais, 1951
Switzerland
Email: jan.vanherle@epfl.ch

Jürg Schiffmann

LAMD
IGM
EPFL
Neuchâtel, Neuchâtel, 2000
Switzerland
Email: jurg.schiffmann@epfl.ch

ABSTRACT

A micro steam turbine with a tip diameter of 15 mm was designed and experimentally characterized. At the nominal mass flow rate and total-to-total pressure ratio of 2.3 kg h^{-1} and 2, respectively, the turbine yields a power of 34 W and a total-to-static isentropic efficiency of 37%. The steam turbine is conceived as a radial-inflow, low-reaction (15%), and partial admission (21%) machine. Since the steam is limited in the system (solid oxide fuel cell), a low-reaction and high-power-density design is preferred. The partial-admission design allows for reduced losses: The turbine rotor and stator blades are prismatic, have a radial chord length of 1 mm and a height of 0.59 mm. Since the relative rotor blade tip clearance (0.24) is high, the blade tip leakage losses are significant. Considering a fixed steam supply, this design allows to increase the blade height, and thus reducing the losses. The steam turbine drives a fan, which operates at low Mach numbers. The rotor is supported on dynamic steam-lubricated bearings; the nominal rotational speed is 175 krpm. A numerical simulation of the steam turbine is in good agreement with the experimental results. Furthermore, a novel test rig setup, featuring extremely-thin thermocouples ($\varnothing 0.15 \text{ mm}$) is investigated for an operation with ambient and hot air at 220°C . Conventional zero and one-dimensional pre-design models correlate well to the experimental results, despite the small size of the turbine blades.

NOMENCLATURE

A	Area in m^2
b	(Channel) width in m
c	Absolute velocity in m s^{-1}
d, D	Diameter in m
d_s	Specific diameter
h	Specific enthalpy in J kg^{-1}
H	Blade height in m
g	Gravitational acceleration in m s^{-2}
l	Length in m
\dot{m}	Mass flow rate in kg s^{-1}
M	Torque in Nm
n_s	Specific speed
p	Pressure in Pa
P	Power in W
r, R	Radius in m
Re	Reynolds number
R_g	Specific gas constant in $\text{J kg}^{-1} \text{K}^{-1}$
s	Specific entropy in $\text{J kg}^{-1} \text{K}^{-1}$
S	Clearance in m
t	(Blade) thickness in m
T	Temperature in K
\dot{V}	Volume flow rate in $\text{m}^3 \text{s}^{-1}$
w	Relative velocity in m s^{-1}
z	Number of blades
α	Absolute blade angle based on the circumference in rad
β	Relative blade angle based on the circumference in rad
δ	Degree of reaction
ζ	Loss coefficient
η	Efficiency
κ	heat capacity ratio
ρ	Density in kg m^{-3}
ϕ	Flow factor
ψ	Stage loading factor
ω	Angular speed in rad s^{-1}

Subscript

1	machine inlet / inlet side test section
2	inlet nozzle inlet
3	inlet nozzle outlet
3.1	volute inlet
4	volute outlet / inducer inlet
5	inducer outlet / turbine stator leading edge
6	stator trailing edge
7	rotor leading edge
8	rotor trailing edge
9	exducer outlet
10	diffuser inlet
11	diffuser outlet
12	machine outlet / outlet side test section
amb	ambient
h	hub
hyd	hydraulic

is isentropic
mech mechanical
s shroud
st static
t total
turb turbine

Abbreviation

AOR anode off-gas recirculation
CFD computational fluid dynamics
FTU fan-turbine unit
LE leading edge
TC thermocouple
TE trailing edge
SOFC solid oxide fuel cell

INTRODUCTION

Within the last two decades, several researchers demonstrated small-scale turbines, mainly for the application in air-to-electrical-power and micro gas turbine generator systems. Epstein [1] suggested a “shirtbutton-sized” gas turbine, featuring a 6 mm radial-inflow turbine with prismatic blades and rotating up to 1200 krpm. The disc-shaped rotor was supported by static and dynamic gas bearings. Kang et al. [2] investigated a “fist-sized” gas turbine with a 12 mm compressor and a back-to-back mounted turbine impeller. The radial-inflow turbine had three-dimensional blades made of silicon nitride and was supported on a shaft with ball bearings. In preliminary tests with ambient air, Kang et al. operated the unit up to 420 krpm, corresponding to 53 % of the nominal speed. Since the compressor performance was the focus of this paper, no experimental results for the turbine were reported. In 2007, Tanaka et al. [3] realized the “worlds-smallest gas turbine” engine with a 17.4 mm radial-inflow turbine. At a rotational speed of 360 krpm and a combustor temperature of 800 °C to 900 °C, a self-sustained Brayton cycle was demonstrated. However, externally pressurized gas film bearings were used; hence, the entire system cannot be considered as fully-self-sustained. In 2012, the Japanese IHI cooperation [4] added dynamic gas film bearings to the unit and demonstrated a fully autonomous operation with an electrical power of 60 W at a rotational speed of 330 krpm.

Several other small-scale turbine systems can be found in the literature, some of which are listed in Table 1. The tip diameters are typically around 10 mm and rotational speeds of up to 500 krpm were reported. The experimentally measured power levels and maximum efficiencies range from one Watt, up to several 100 Watts and from 8 % up to 58 %, respectively. The rotational speeds in Table 1 correspond to the listed power and efficiency measurements and not to the nominal speed. In some cases, it was not reached due to technical limitations or the highest efficiency was reached at lower rotor speeds.

In 2003, Peirs et al. [5] presented a 9.9 mm axial impulse turbine with an optimal rotational speed of 420 krpm. Due to bearing lim-

itations, the turbine was then designed for 210 krpm. However, due to further limitations of the electrical generator, the highest overall efficiency (10.5 %) was reached at 100 krpm, yielding an isentropic efficiency of 18.4 % and a shaft power of 28 W. In a second step Peirs et al. implemented “better ball bearings”, adjusted the gap between the nozzle disc and rotor, and injected hot air (up to 360 °C) instead of ambient air. The turbine reached overall efficiencies of up to 16 %.

Arnolds et al. [6] coupled an off-the-shelf dental drill to a magnetic generator. A maximum power of 1.1 W at a rotational speed of 200 krpm was reached. The exact turbine inlet mass flow rate was not measured, but estimated to 45 l min^{-1} (ambient air), which leads to an estimated overall efficiency of 8 %.

Krähenbühl et al. [7] tested a 9.5 mm axial impulse turbine, featuring prismatic blades with a height of 0.5 mm. The tip clearance was set to 0.1 mm. The power loss of the generator and the ball-bearing-supported shaft were measured with coast-down tests (13 W at 500 krpm). This allowed to determine the turbine isentropic efficiency with the overall efficiency, based on the electrical power output. Krähenbühl et al. also intended to measure the turbine power and efficiency with the inlet and outlet enthalpies. However, they failed in doing so, since the turbine was not sufficiently insulated from the thermal losses of generator and bearings. The highest overall efficiency of 24 % was reached at 370 krpm, corresponding to a turbine efficiency of 28 %. The turbine power was estimated to 143 W.

Later, Krähenbühl et al. [8] presented a 10.5 mm radial-inflow turbine geometry, based on three-dimensional blades and a blade tip clearance, that is “as small as possible” (no exact value is given in the reference). The ball-bearing-supported rotor reached rotational speeds in excess of 600 krpm for a shaft diameter of 3.175 mm. The maximum electrical power of 170 W was reached at 495 krpm, resulting in an overall and turbine efficiency of 43 % and 52 %, respectively.

Sato et al. [9] demonstrated a “palm-sized” 10 mm radial-inflow low-reaction turbine based on prismatic blades manufactured from Silicon. The rotor had 40 blades with a radial chord of 1 mm, a blade height of 0.2 mm, and a running blade tip clearance of smaller than 0.025 mm, which was adjusted with shims. Without turbine, the ball-bearing supported rotor was tested up to 475 krpm (106 % of the nominal rotational speed) by using the generator as an electrical motor. However, due to axial load limitations, the turbine was tested only up to 360 krpm. Due to heat conduction problems and difficulties to measure all thermodynamic properties for such a micro device, the power and total-to-static isentropic efficiency were estimated. The actual turbine inlet temperature was corrected with the heat addition, resulting from the ball-bearings and the electrical generator. An isentropic efficiency of 47 % and a turbine power of 37 W was measured. This corresponds to an electrical power of 30 W (generator efficiency of 81 %).

Fu et al. [10] presented a 10.6 mm radial-inflow turbine with forward-curved prismatic blades, similar to the design of Sato et al. [9]. Due to the higher radial chord length of 2 mm (estimated from figure 4 of the reference), the number of blades is lower (11) than the design by Sato et al. (40). The blade height is 1 mm and no information on the blade tip clearance is given. The static-gas-bearing-supported rotor was operated up to 80 % of the nominal rotational speed (450 krpm). Since no generator was used, the turbine power was determined with the measured inlet and outlet enthalpies of the load compressor (assumption of a mechanical efficiency of 100 %). A total-to-static

isentropic efficiency of 57 % was reported, resulting in an estimated power of 96 W (mass flow rate of 1.5 g s^{-1} and pressure ratio of 2.93). This corresponds to the highest isentropic efficiency reported in literature for a ~ 10 mm turbine, despite the coarse manufactured prismatic turbine blades. However, the power and efficiency measurement with a generator is typically more reliable than a thermodynamic approach.

All previously described experimental setups used ambient air, except for Arnold et al. [6] (ambient nitrogen) and Peirs et al. [5] (hot air). Considering water vapor, the literature offers three different approaches of small-scale steam turbines: (1) The company Green Turbine [11] offers an axial impulse steam turbine coupled to a generator with a maximum electrical power of 1400 W. (2) Kim et al. [12] investigated an array of Hero turbines (also known as aeolipe) with a diameter of 144 mm, reaching an electrical power of 1500 W, a mechanical power of 4650 W, and a total-to-static isentropic efficiency of 20 %. (3) Placco et al. [13] investigated a 70 mm Tesla turbine and measured a mechanical power of 18 W (dynamometer) and an isentropic efficiency of 25 %.

According to the authors' knowledge, no experimental characterization of a micro steam turbine was published so far, except for the unit presented in this paper: a micro radial-inflow, partial-admission (0.21), and low-reaction (0.15) steam turbine. The 15 mm turbine propels a 8 mm shaft, that is supported on dynamic steam-lubricated bearings and rotates at 175 krpm (nominal rotor speed). Such a device is particularly interesting for off-gas recirculation devices in solid oxide fuel cell (SOFC) systems.

ADVANTAGES OF STEAM-TURBINE-DRIVEN OFF-GAS RECIRCULATION DEVICES FOR SOFC SYSTEMS

Wagner et al. [14] simulated and optimized a 10 kW_e SOFC system (cogeneration of electricity and heat) with an electrically-driven anode off-gas recirculation (AOR) fan, as shown in Figure 1 (A). The advantages of the AOR are: (1) a higher SOFC system efficiency, (2) a higher SOFC stack lifetime, and (3) a water-neutral operation of the system. Additionally, the AOR fan is lubricated on dynamic gas bearings; hence, it operates oil-free. This is of importance, since the SOFC stack cannot tolerate contamination with oil or grease. However, this AOR fan concept has a major limitation: the electric motor of the AOR fan and the explosive anode off-gas, which contains hydrogen and carbon monoxide, could lead to failures.

As addition to this conventional AOR concept in Figure 1 (A), Wagner et al. [15] replaced the electrical motor with the previously mentioned micro steam turbine. This addition is shown in Figure 1 (B). The advantages of such a steam-driven AOR fan are: (1) explosion-proof operation, due to the lack of electrical components, (2) no external inert gas supply, since the shaft is dynamically lubricated on steam, and (3) no leakage of toxic carbon monoxide to the turbine side. Additionally, the system efficiency is increased, since the pump electrical power is decreased compared to an electrically-driven AOR fan. The recovery of the SOFC system excess heat is sufficient to realize the steam generation for the turbine; hence, the AOR fan is steam-, as well as thermally-driven.

Wagner et al. [15] realized this novel SOFC system, including a prototype 6 kW_e SOFC stack from the company SOLIDpower and the steam-driven AOR fan. They reported an increase of the SOFC system electrical gross DC efficiency and DC power by 10 % and 540 W_e , respectively. At this operational point, the steam turbine rotated at 169 krpm; its total-to-static isentropic efficiency and power

were estimated to be 28 W and 40 %, respectively. However, the authors stated that the turbine power and efficiency measurement is challenging, due to heat conduction.

NATURE OF THE ISSUE

Steam-driven micro fans are particularly interesting for the application in SOFC systems with anode off-gas recirculation. Such devices can significantly improve the system lifetime and efficiency. However, the literature does not provide design guidelines for such a micro steam turbine. The design is challenging, since the turbine losses are increased (small-scale limitations). Additionally, the turbine and fan operate at high and low Mach numbers, respectively, which leads to different optimal speeds. The implementation of a gearing mechanism is not feasible, since the required dynamic gas bearings have a low tolerance to misalignment due to the low load capacity.

Previously characterized micro turbines were connected to an electrical motor. Thus, the turbine power and efficiency could be measured accurately. Krähenbühl et al. [7] compared a thermodynamic measurement approach with one using an electrical motor and they reported an infeasible measurement due to heat conduction. Sato et al. [9] used first thermodynamic law considerations to estimate the turbine inlet temperature by adding the measured bearing and electrical motor losses.

Fu et al. [10] used a load compressor instead of an electrical motor. They measured the compressor efficiency and assumed 100 % mechanical efficiency to estimate the turbine efficiency. Since the presented steam-driven AOR fan has a low mechanical efficiency ($\sim 60\%$) and no electrical motor, only the thermodynamic measurement approach on the turbine side is feasible. However, the literature lacks of guidelines for an accurate power and efficiency measurement of such a micro (steam) turbine.

Additionally, the validity of the micro (steam) turbine pre-design with conventional zero- and one-dimensional models is unclear.

OBJECTIVES AND SCOPE OF THE PAPER

This paper has therefore three objectives: (1) Giving design guidelines by outlining the design of such a micro steam turbine, that drives a fan, (2) characterizing this turbine and giving measurement guidelines, and (3) validating classical zero- and one-dimensional pre-design models for this specific turbine design.

A micro steam turbines is, therefore, designed, manufactured, and characterized. A novel test rig setup with extremely-thin $\varnothing 0.15$ mm thermocouples is presented and evaluated both for ambient and hot air (220°C). The results of a conventional test rig setup with $\varnothing 1.5$ mm thermocouples and the novel setup are compared towards a computational fluid dynamic (CFD) simulation. Finally, non-dimensional similarity concepts and one-dimensional loss models, conducted from standard-sized turbines ($Re_{d_{hyd}} > 1e^5$), are compared to the experimental and numerical results of the micro steam turbine, which allows to validate these concepts for this specific case.

STEAM TURBINE DESIGN SUMMARY

The radial-inflow turbine design is inspired by the work by Jovanovic [16] and Sato et al. [9]. It follows three iterative steps, taking into account technical limitations due to manufacturing and assembling:

(1) A high-level systems simulation and optimization of the entire SOFC system similarly to the methodology described by Wagner et al. [14] allows to determine the turbine tip diameter, rotational speed, total-to-static isentropic efficiency, and admission. This system-based simulation includes a model of the waste-heat-driven radial anode off-gas recirculation fan and the driving steam turbine, based on non-dimensional similarity concepts by Balje [17]. The steam-lubricated journal and thrust bearing design is included to estimate the shaft diameter and the bearing losses.

(2) A classical mean-line analysis allows to further specify the turbine geometry. It determines the blade metal angles, the blade height, and the number of blades. The turbine efficiency is estimated with loss correlations by Soderberg [18]. The partial admission losses (pumping and filling-emptying losses) are estimated with correlations by Roelke (chapter 8 in [19]) and Stenning [20], respectively.

(3) Manual iterations with a steady-state single-passage CFD simulation refine the turbine rotor and stator geometry (blade metal angles, thickness distributions, chamber mean-lines, and number of blades). The admission is chosen in such way, that the turbine can overcome its estimated partial admission losses, the estimated bearing and shaft windage losses, and deliver the required fan power.

The excess heat for steam generation is limited in the SOFC system. Thus, the steam turbine was designed to achieve a high specific power (P/\dot{m}). A high turbine inlet pressure leads to a high Mach number in the stator, and thus to a high specific power. However, an accurate Laval nozzle is necessary to realize Mach numbers beyond 1. The authors rejected such a design, since it is challenging to manufacture at a micro scale. Further rejected complex designs include a multi-stage Parsons turbine, a Tesla turbine, and a Ljungström turbine. The realized design uses a convergent stator and operates at choked conditions. The semi-vaneless space after the nozzle throat acts as a diverging nozzle; hence, local Mach numbers of up to 1.3 are possible. A low-reaction turbine design was chosen, due to several advantages:

- **High-power:** A high turning angle leads to a high specific power, but to a lower isentropic efficiency.
- **Low thrust force:** The turbine impeller hub static pressure profile, and thus the thrust force, is reduced.
- **Partial-admission:** Only a low-reaction turbine is capable of operating efficiently in partial-admission mode. The partial-admission design adds more design flexibility, which is of particular interest when the blade features become very small. Partial admission allows (1) increasing the turbine radius while the blade height remains constant, (2) increasing the blade height while the turbine radius remains constant, or (3) a combination of the two. A higher radius increases the turbine specific enthalpy (at constant rotational speed). An increased blade height decreases the relative blade tip clearance, and thus increases the turbine isentropic efficiency (not considering partial-admission losses).
- **Low turbine-to-fan leakage rate:** The pressure difference between the turbine and the fan trailing edge (TE) is lower, which leads

to a lower steam leakage from the turbine side, through the housing of the unit, to the AOR fan.

- **Low blade tip clearance leakage:** A low-reaction turbine design leads to a lower pressure difference between the blade suction and pressure side, which is favorable for a reduced tip leakage loss [19]. Since the blade height is small (0.59 mm) and the turbine blade tip clearance relatively high (0.133 mm), the blade tip clearance loss is the most pronounced secondary flow loss in this design.

Classical design approach: Lewis [21] provides correlation for optimal turbine design in terms of the flow factor

$$\phi_i = \frac{c_{m,i}}{u_i} \quad (1)$$

the stage loading factor

$$\psi = \frac{4\Delta h_{tt}}{d_8^2 \omega^2} \quad (2)$$

and the turbine degree of reaction.

$$\delta = \frac{\Delta h_{stst,rotor}}{\Delta h_{stst,stage}} \quad (3)$$

The flow factor at a turbine section (i) is the ratio of the meridional velocity ($c_{m,i}$) to the circumferential velocity (u_i), both based on the mean radius of the section. The stage loading factor is the ratio of the total-to-total specific enthalpy difference (Δh_{tt}) to the square of the circumferential velocity at the rotor blade TE mean diameter ($u_8 = \omega \frac{d_8}{2}$). The degree of reaction is the ratio of the static-to-static specific enthalpy difference of the rotor ($\Delta h_{stst,rotor}$) to the static-to-static specific enthalpy difference of the stator and rotor ($\Delta h_{stst,stage}$).

Design challenges: The fan has a low pressure rise and, therefore, a relatively low blade tip Mach number. Thus, the fan rotational speed is relatively low, which limits the turbine efficiency. The integrated system optimization suggests a high fan specific speed

$$n_s = \omega \frac{\sqrt{V_8}}{\Delta h_{is,tst}^{0.75}} \quad (4)$$

of 1.1, and thus a low fan isentropic efficiency, in order to increase the turbine efficiency.

The realized turbine design does not operate in the optimal design region, as suggested by Lewis [21]. Due to the low blade tip Mach number of 0.25, the measured flow coefficient (based on the rotor leading edge) and the stage loading coefficient (based on the rotor TE) are 1.2 and 3.7, respectively, for the nominal operation (steam at 220 °C). These values are higher than the recommended values of 0.5-0.8 and 1.6-2.0, respectively, for a turbine with a reaction of 0.15.

In summary, the three design challenges for this specific steam turbine are: (1) a high relative Mach number at the turbine rotor blade leading edge (LE), due to high stage loading factor/low tip speed, (2) manufacturing limitations, i.e., relatively thick rotor blade edges, and (3) a high relative rotor blade tip clearance.

Baseline design: Table 2 lists all geometrical turbine design parameters. Figure 2 shows the turbine volute, inducer, and stator. Figure 3 (B) shows the turbine inducer, stator, and rotor and (A) a zoom of the stator and rotor. The component design is described as follows:

Volute (section 3.1 to 4): Figure 2 shows the tunnel-type volute between section 3.1 and 4. The first part of the turbine volute was manufactured with a spherical milling tool. However, the size of the tool was limited to 0.5 mm, such that the last part (starting from section 3.2 in Figure 2) was manufactured with a planar milling tool and approximated flat surfaces. Figure 2 (E) indicates its cross-section, which consists of a half circle ($R_{3,1}=2$ mm) and a rectangle ($2R_{3,1} = 4$ mm and $b_{3,1} = 0.7$ mm). The volute width is equal to the stator blade channel width ($b_{3,1} = b_{3,2} = b_4 = b_5 = b_6 = 0.7$ mm). The turbine volute was designed for a constant angular momentum ($rc_u = \text{const.}$), yielding a homogeneous distribution of the fluid to the turbine inducer inlet (section 4). It features the same admission ratio ($\frac{13}{61}$) as the turbine stator. In first approximation, the absolute flow angle at the volute outlet (α_4) is independent of the fluid properties. It is a function of the volute inlet and outlet area ($A_{3,1}$ and A_4 , respectively) and the radii ($r_{3,1} = r_4 + R_{3,1}$ and r_4 , respectively).

$$\alpha_4 = \arctan\left(\frac{r_{3,1}}{r_4} \frac{A_4}{A_{3,1}}\right) = 33^\circ \quad (5)$$

A numerical investigation of this specific turbine volute by Font [22] suggested good correlation. The deviation between the numerical and analytical value of α_4 was up to $+1^\circ$ for this specific case; hence, eq. (5) is a good approximation.

Inducer (section 4 to 5): Ideally, the inducer guides the flow to the stator, without turning it (Figure 3 (B)). However, the absolute flow angle (α) is not constant between the inducer inlet (section 4) and outlet (5). Due to the relatively small channel width of 0.7 mm, the frictional losses of the walls reduce the fluid momentum; hence, the absolute velocity circumferential component does not strictly follow the $rc_u = \text{const.}$ correlation. According to a steady single-passage CFD simulation, the flow angle increases by up to 10° between the turbine inducer inlet (4) and the stator LE (5) for steam at 220 °C. Thus, the sidewall geometry is estimated with a CFD simulation,

based on the nominal point.

Stator (section 5 to 6): The stator blade LE and TE angles ($\alpha_{5,blade}$ and $\alpha_{6,blade}$, respectively) are 43.7° and 22° , respectively. The flow deviation at the stator TE is low, since the stator solidity is high. The blade solidity based on the turbine stator TE ($\frac{r_5-r_6}{2\pi r_6}$) is 1.26 and 2.42 using the actual chord length (1.93 mm). The blade aspect ratio ($\frac{H_5}{r_5-r_6}$) is 0.7 and 0.36 using the actual blade chord length (1.92 mm). Some geometrical parameters are limited by manufacturing: the stator blade TE thickness is 0.08 mm and the stator blade height is 0.7 mm (maximum length of 0.8 mm for the 0.2 mm milling tool). The selected stator blade TE thickness and blade height are challenging to manufacture, and some stator blades show plastic deformation at the blade TE due to the manufacturing process (Figure 3 (A)).

Rotor (section 7 to 8): The turbine rotor blade thickness and blade angle distribution is based on a modified NACA profile of the primary series from the technical note 3802 [23]. The selected blade turning angle is 102° ($\beta_{7,blade} - \beta_{8,blade}$), whereas the blade stagger angle is 6.6° . The NACA technical note 3802 provides recommendations for the LE and TE radii. A LE and TE radius divided by the chord length of 4.4 % and 1 %, respectively, are recommended. This would lead to a LE and TE radius of 0.045 mm and 0.01 mm, respectively. However, such small radii are not possible to manufacture with the selected method (milling) and for the selected material (stainless steel). For the proposed turbine rotor blade design, the LE and TE radii are 0.09 mm and 0.08 mm, respectively; nearly eight-times higher than the recommendation from the NACA technical note.

As a result, the turbine blade design is challenging for three reasons: (1) The high power density requires high blade turning, (2) the relative Mach numbers at the rotor LE is relatively high, due to a high stage loading factor, and (3) the acceleration at the turbine rotor LE is high due to a relatively high LE radius. Thus, the original NACA primary profile from technical note 3802 [23] lead to increased separation at the rotor blade suction and pressure side (depending on the blade incidence), as well as to a rapid acceleration and deceleration at the thick blade LE. To limit these negative effects, the maximum normal layer thickness was shifted from the initial 20 % chord location to 35 %. In addition, the normal layer thickness was set at 0.21 mm and the blade turning at the turbine LE was decreased.

The high relative blade tip clearance increases the turbine secondary flows, leading to a higher flow deviation at the turbine TE. Since this parameter has a significant impact on the turbine power and efficiency, it was validated with dimensional measurements: (1) The average blade height was determined to 0.586 mm. (2) The average turbine rotor blade tip clearance at zero speed was determined to 0.133 mm (s_{tip} in Figure 4 (C)). (3) The axial offset between the rotor and the stator hub surface, which is the reference for the measurement, is -0.019 mm at zero speed. Although the unit uses a shim (precise shim in Figure 4 (C)), the alignment to the micrometer is challenging. Wagner et al. [24] measured the thrust bearing clearance for this unit at ambient conditions and estimated it for nominal conditions (200 °C). Due to the axial motion of the rotor (0.01 mm), the rotor and stator hub misalignment increases from the initial -0.019 mm to -0.029 mm at 175 krpm. Consequently, the turbine channel width and the blade tip clearance increase with speed from 0.719 mm to 0.729 mm and from 0.133 to 0.143 mm, respectively. This corresponds to relative running blade tip clearance ($\frac{s_{tip}}{H_7}$) of 0.24.

The selected number of turbine rotor blades (59) is a trade-off between deviation, blade profile losses, and partial-admission losses. A high blade number is beneficial for a low deviation and for low partial-admission losses, but increases the profile losses. The selected blade solidity based on the turbine rotor TE ($\frac{r_7-r_8}{2\pi r_8} 59$) is 1.44 and 1.46 using the actual chord length (1.01 mm).

Exducer and diffuser (section 8 to 11): The turbine exducer hub and shroud are based on circular surfaces with a radius of 3.275 mm and 2.35 mm, respectively. Considering a full-admission exducer, the flow would be accelerated, since the area at the exducer inlet ($\pi(d_{9s} + 2.35 \text{ mm})b_8$) is higher than the area at the exducer outlet ($\pi(d_{9s}^2 - d_{9h}^2)$). However, the partial-admission exducer ($\frac{13}{61}$) expands the flow, which leads to a diffusion. The turbine rotor TE is thus designed in such way that the flow exits the rotor in a nearly 90° angle to limit the swirling motion of the flow, and thus the losses. At the machine outlet (section 10 to 11), the flow diffuses in a diffuser from a 8 mm diameter to a 12 mm diameter. The diffuser length is 20.8 mm.

MEASUREMENT SETUP

The test rig and measurement equipment used for the experiments, are similar to the ones described by Wagner et al. [24]. Figure 4 shows a piping and instrumentation diagram of the entire fan-turbine unit test rig, including the fan and the turbine measurement sections. The figure is divided into (A) a schematic overview of the auxiliary equipment outside the electrical oven, (B) a to-scale side view of the fan and turbine measurement section, that is placed inside the oven, (C) a zoomed to-scale view of the turbine and (D) fan measurements, and (E) a picture of the actual implementation with the glass fiber insulation tapes.

Tests with ambient/hot air (option 1 on the bottom of Figure 4) and with hot steam (option 2) were performed. Considering option 1, pressurized and dehumidified air at ambient temperature was controlled with a manual valve. The mass flow rate was determined with an *Emerson* D S006S Coriolis mass flow meter (measurement uncertainty of $\pm(0.002 + \frac{0.006}{\dot{m}}) 100\%$ on the read, \dot{m} in kg h^{-1}). Its position is marked with the sensor “F” in Figure 4 (A). Considering option 2, A *KNF* SIMDOS10 membrane pump ($\pm 0.12 \text{ kg h}^{-1}$) drew the deionized water from a tank through a mesh filter to the *EBZ* evaporator and to the turbine. The evaporator could also be used to heat the ambient air. At the turbine outlet, the air or water vapor was expanded to the ambient (no condenser). The fan drew air from the ambient or from the oven through the bellmouth (Figure 4 (B) at the top). In order to avoid a sub-atmospheric pressure in the oven, heated air was injected horizontally at the bottom of the oven (Figure 4 at the bottom). This allowed for a lower vertical temperature gradient and a conservation of the mass within the oven.

The shaft torque could not be measured and no generator was integrated. Thus, the turbine power was determined with the inlet and outlet total enthalpies ($\dot{m}h_t$), assuming zero turbine-to-fan leakage and neglecting heat conduction and convection effects. The static gauge pressures (marked as “P” sensors in Figure 4) were measured with a *Scanivalve* DSA 3217 (6.9 bar) with a verified measurement uncertainty of $\pm 0.02\%$ on the full scale ($\pm 0.7 \text{ mbar}$). The ambient pressure was measured with a *Lufft* Opus 20 ($\pm 0.5 \text{ mbar}$). Temperatures were measured with class 1 k-type thermocouples (calibrated, $\pm 0.5^\circ\text{C}$), marked as “T” sensors in Figure 4. The rotational speed was measured with a *Philtec* D 20 optical probe.

This sensor has a measurement uncertainty of ± 0.5 krpm (sampling rate of 50 kHz) and is marked with an “R” in Figure 4.

The turbine inlet and outlet measurement sections (1 and 12 in Figure 4 (B), respectively) each featured two $\varnothing 1.5$ mm thermocouples (at 180°) and four evenly-distributed static pressure taps (pneumatically-averaged). Thermocouple 1 (TC1) at the inlet section was wall-mounted and thermocouple 2 (TC2) was immersed two-times the diameter (3 mm) into the 6 mm tube. Thermocouples 5 and 6 (TC5 and TC6) at the outlet side test sections were also immersed two-times the diameter (3 mm) into the 12 mm tube. These four thermocouples are robust, easy-to-install, and easy-to-seal. This conventional test rig setup is compared to a novel set up featuring two $\varnothing 0.15$ mm thermocouples. Thermocouple 3 (TC3) was inserted into the turbine volute. A picture of the actual implementation is shown in Figure 2 (A) and a schematic view is shown in Figure 4 (B) and (C). Thermocouple 4 (TC4) was inserted down-stream of the turbine TE, as shown in Figure 2 (C), as well as Figure 4 (B) and (C). Both thermocouples were inserted via a 0.5 mm hole. TC3 and TC4 protruded 1 mm and 0.5 mm, respectively, that corresponds to 6.7 and 3.3-times the diameter, respectively. Sealing was achieved with a *Loctite* EA 9497 glue. Although, the test rig setup worked for hot air at 220°C , two problems were encountered for the hot steam setup at 220°C : (1) A leakage occurred due to the corrosiveness of the steam, and (2) thermocouple 4 broke (Figure 2 (C)). The authors assume water droplets in the steam during the system startup as possible reason for the defect.

Besides the inlet and outlet static gauge pressure, the rotor-stator pressure was measured with a $\varnothing 0.15$ mm half circle tap at the shroud surface, as shown in Figure 2 (B). The static pressure at the turbine section 9 was measured with a 0.5 mm pressure tap, as shown in Figure 2 (D) and Figure 4 (B) and (C).

TURBINE POWER AND EFFICIENCY DEFINITION

Two different power definitions were investigated.

$$P_1 = \dot{m}_1 \Delta h_{t,1} = \dot{m}_1 \left(h_t(T_{TC2}, p_{t,4}) - h_t \left(\frac{T_{TC5} + T_{TC6}}{2}, p_{amb} \right) \right) \quad (6)$$

$$P_2 = \dot{m}_1 \Delta h_{t,2} = \dot{m}_1 (h_t(T_{TC3}, p_{t,4}) - h_t(T_{TC4}, p_{amb})) \quad (7)$$

P_1 is based on the $\varnothing 1.5$ mm thermocouple at the inlet (T_{TC2} , inserted 2d) and the averaged temperature of the two $\varnothing 1.5$ mm thermocouples at the outlet (T_{TC5} and T_{TC6} , both inserted 2d). P_2 is based on the two $\varnothing 0.15$ mm thermocouples at the volute (T_{TC3}) and after the turbine TE (T_{TC4}). The measured temperatures are corrected with a recovery factor according to the correlations proposed by Hirschberg et al. [25]. However, this is only relevant for TC4, since here high Mach numbers are reached ($M > 0.3$). Both power definitions use the estimated total pressure at turbine section 4 (Figure 2, Figure 3, and Figure 4 (C)) and the measured ambient pressure (p_{amb}). The pressure loss between the inlet section 1 and section 4 is estimated with an analytical model by Font [22] for this specific volute geometry. Font verified the model with CFD simulation (correlations within ± 1 mbar); the pressure loss is below 15 mbar for all operational points.

Similarly, the total-to-static isentropic efficiency 1 and 2 is defined for the two cases.

$$\eta_{is,tst,1} = \frac{\Delta h_{tt,1}}{\Delta h_{is,tst,1}} \quad (8)$$

$$\eta_{is,tst,2} = \frac{\Delta h_{tt,2}}{\Delta h_{is,tst,2}} \quad (9)$$

The turbine total-to-static isentropic specific enthalpy difference 1 and 2

$$\Delta h_{is,tst,1} = (h_t(T_{TC2}, p_{t,4}) - h_{st}(s(T_{TC2}, p_{t,4}), p_{amb})) \quad (10)$$

$$\Delta h_{is,tst,2} = (h_t(T_{TC3}, p_{t,4}) - h_{st}(s(T_{TC3}, p_{t,4}), p_{amb})) \quad (11)$$

uses the total inlet total temperature (T_{TC2} and T_{TC3} , respectively), the total pressure at section 4 ($p_{t,4}$), the ambient pressure (p_{amb}), and the entropy at the inlet ($s(T_{TC2}, p_{t,4})$ and $s(T_{TC3}, p_{t,4})$, respectively).

Wagner et al. [15] suggested a corrected turbine efficiency and power

$$\eta_{turb,corr} = \frac{\eta_{FTU}}{\eta_{mech}\eta_{fan}} \quad (12)$$

$$P_{turb,corr} = P_{turb} \frac{\eta_{turb,corr}}{\eta_{turb}} \quad (13)$$

based on the measured fan-turbine unit efficiency (η_{FTU}), the fan efficiency (η_{fan}), and the estimated mechanical efficiency (η_{mech}). The fan-turbine unit efficiency

$$\eta_{FTU} = \frac{\dot{m}_{fan} (h_{is,t,fan,out}(p_{t,fan,out}, s_{fan,in}) - h_{t,fan,in})}{\dot{m}_{turb} (h_{t,turb,in} - h_{is,t,turb,out}(p_{t,turb,out}, s_{turb,in}))} \quad (14)$$

depends on the fan and turbine inlet conditions, as well as on the total pressure at the outlet. It is more accurate to measure, since the heat conduction effects are reduced at the inlet sections. Compared to the turbine side, the fan efficiency (η_{fan}) is more accurate to measure, since heat conduction is reduced due to: (1) lower fluid velocity and thus lower heat transfer coefficients, (2) lower area-to-volume ratio, and (3) lower temperature gradients. The mechanical efficiency (η_{mech}) of the gas-film-lubricated shaft is estimated with a model by

Demierre et al. [26]. They compared the model to rotor run-out measurements of a microrcompressor-turbine unit and it correlated within a $\pm 10\%$ band. The model is based on the measured shaft rotational speed, the bearing temperature, and the housing pressure.

The turbine reaction

$$\delta \approx \frac{p_{rotor-stator} - p_{amb}}{p_{st,1} - p_{amb}} \quad (15)$$

is estimated with the measured turbine rotor-stator static pressure ($p_{rotor-stator}$, measured with tap in Figure 2 (B)), the ambient pressure (p_{amb}), and the turbine inlet static pressure at section 1 ($p_{st,1}$), as shown in Figure 4 (B).

NUMERICAL SETUP

The commercial software *Ansys CFX* 19.2 was used for the steady and transient CFD simulation. Since the simulation accounts only for one passage, the empty-filling losses at the end and the start of the admission, respectively, and the pumping effect of the non-admission turbine blades are not taken into account.

SP Domain: Figure 5 shows the simulation domain, consisting of the turbine inducer (Figure 3 (B) on the top and Figure 4 (C)), the turbine stator, the turbine rotor, and the turbine exducer until turbine section 9, as shown in Figure 3 (B) and Figure 4 (C). The turbine lock nut (Figure 4 (C)) is modeled as round, although it features a hexagon for tightening. The rotor and the stator are aligned in such way, that the turbine power of the steady simulation has a comparable result to the one-period-averaged power of the transient simulation.

Grid generation: A structured mesh is generated with the “ATM topology” of *ANSYS TurboGrid*, where the first cell height is selected to achieve an average y^+ value of 1. The time step for the transient simulation is chosen to achieve a root-mean-squared Courant number of lower than one (500 steps per blade passing). The turbine tip clearance is assumed as constant (0.143 mm) for all cases (mechanical or thermal deformation is thus neglected) and modeled with 30 layers. In total, the mesh has one million hexahedral elements.

Boundary conditions: As listed in Table 2, the stator has 12 blades and features an admission of $\frac{12+1}{61} = 0.21$. The single passage simulation features a periodic boundary condition for each domain, thus in total there are $4 \cdot 2 = 8$ periodic boundary conditions. The turbine rotor has 59 rotor blades and features fluid-to-fluid frozen rotor interface with pitch change between the stator-rotor domain (rotor-stator interface #1 in Figure 5). The inlet boundary condition (turbine section 4) is the total temperature (from TC3) and the total pressure at section 4 (total pressure of section 1 minus the estimated pressure loss), as well as the absolute flow angle ($\alpha_4 = 33.4^\circ$). The outlet boundary condition (turbine section 9) is the measured area-averaged static pressure at section 9 (Figure 2 (D)), Figure 2 (B), and Figure 4 (C). Hence, the mass flow rate through the passage is the result of the simulation. The rotor shroud is simulated as counter-rotating wall. The stationary exducer domain hub assumes a rotating wall with the rotational speed of the rotor domain. All walls are modeled as adiabatic and smooth. The simulation does not account for the axial offset (negative step between the stator and

the impeller hub surfaces) at the nominal speed of -0.029 mm.

Solver setup: A compressible and non-isothermal ideal gas is assumed. The advection scheme is set to high resolution. The SST turbulence model by Menter [27] with a medium turbulence intensity of 5% at the inlet boundary condition (section 4) is selected.

Data extraction: The turbine power is evaluated as the impeller torque (blades and hub) and the exducer hub torque around the rotational axis multiplied with its angular velocity, the number of blades (59), and the admission (0.21). The mass flow rate is evaluated with the inlet passage mass flow rate multiplied with 13 ($z_{stator} + 1$). The efficiency is evaluated as the total-to-total specific enthalpy difference (mass-flow-averaged values at section 4 and 9) divided by the total-to-static isentropic specific enthalpy difference from eq. (11). The turbine reaction is calculated according to eq. (15), where the rotor-stator static pressure is evaluated as the line-averaged static pressure at the turbine shroud at the rotor-stator interface #1 in Figure 5.

COMPARISON OF THE EXPERIMENTAL RESULTS TOWARDS THE NUMERICAL RESULTS

The turbine was investigated both at steady and transient operation, with ambient air, hot air, and water vapor.

Ambient air (transient): The transient behavior of the thermocouples is outlined for a case with ambient and dehumidified air. Eight thermocouples are investigated: three at the turbine inlet (TC1-TC3), three at the turbine outlet (TC4-TC6), and two at the shaft, which measure the bearing temperature (TB1 and TB2). All positions of these eight temperature sensors are indicated in Figure 4 (B) and (C) with a “T”.

Figure 6 shows two transient operations (turbine startup and coast-down) and a steady operation at the nominal rotational speed (175 krpm) between minute 6.0 and 17.1. At the start, the temperatures of TC1-4 and TB1-2 were within $\pm 0.1^\circ\text{C}$ at 24.4°C (ambient temperature). TC5 and TC6 indicated a slightly lower temperature of 23.5°C , due to a previous turbine test and the resulting cooling effect of the outlet side test section. Until the beginning of the steady-state operation at minute 6, the TC4 rapidly decreased to 1.3°C (corrected temperature of 2.9°C), whereas TC4 and TC5 indicated 15.2°C . This suggests a heat conduction and convection of 16 W, based on first law considerations. The wall-mounted thermocouple at the inlet (TC1) still indicated the ambient temperature from the beginning (24.4°C). The 2d-immersed TC2 indicated consistently a lower temperature of 0.1°C than the wall-mounted TC1. The thermocouple in the volute (TC3) dropped to 23.9°C (corrected temperature of 24.2°C). At this point, the difference between TC1 and TC3 was 0.3°C , either due to a cooling effect in the volute (expansion in the turbine) or due to an inaccurate recovery factor. After 11.1 minutes of steady operation, TC5 and TC6 indicated a non-steady temperature of 7.6°C , and thus a power and a total-to-static isentropic efficiency of 21 W and 24%, respectively. According to the authors' experience, it can take up to 90 min to reach a steady operation for TC5 and TC6. TC3 indicated a steady temperature (0°C and 1.6°C for the raw and corrected temperature, respectively), and thus a steady power and an efficiency of 28 W and 33%, respectively. The results of the CFD simulation suggest an outlet temperature of -5.9°C , a power of 32 W, an efficiency of 45%, and a mass flow rate of 3.8 kg h^{-1} (experiment 4.6 kg h^{-1}).

The bearing temperatures close to the fan and turbine (TB1 and TB2, respectively) reached 32.1°C and 30.5°C , respectively. TB2 is

lower due to the cooling effect on the turbine-side. During the coast-down starting at minute 17.1, the mass flow rate to the turbine was decreased to zero until minute 17.45. TC4 rapidly increased to 18 °C. At minute 17.4, the temperature in the volute started to drop from 23.1 °C to 19.9 °C, since the turbine acted as a “fan” and pumped the cold air upstream into the volute.

Turbine characteristic: Figure 7 shows the measured and simulated turbine characteristic, including the reduced inlet mass flow rate ($\dot{m}\sqrt{T_{t,1}}p_{t,1}^{-1}$ in $kg\,h^{-1}\sqrt{Kbar}^{-1}$), the reaction according to eq. (15), the power, the total-to-static isentropic efficiency, and the total-to-static pressure ratio. The pressure ratio of the single passage CFD simulation (dotted lines) is identical to the experiments due to the selected boundary conditions. The turbine characteristic was investigated for the following fluids: ambient air (AA, green circles), hot air (HA, red squares), and water vapor (WV, blue triangles). For all three fluids, the power and efficiency was measured with the conventional $\varnothing 1.5$ mm thermocouples according to eqs. (6) and (8), respectively (solid lines). Additionally, the power and efficiency was measured with the $\varnothing 0.15$ mm thermocouples according to eqs. (7) and (9), respectively, for the ambient air and hot air case (dashed lines). Figure 7 also indicates the corrected turbine efficiency and power (thin solid lines) according to eqs. (12) and (13), respectively, for the hot air and the water vapor case.

Control and limitations of the test conditions: The recirculation fan (shown in Figure 4 (B) at the top) and the windage losses of the shaft and the dynamic gas bearings were the load for all turbine tests. The turbine speed was controlled with the valve 1 at the turbine inlet for the operation with hot and cold air or the pump for the operation with steam. The fan was controlled with the valve 2 at the fan outlet. These components are shown in Figure 4 (A). The valve 2 can throttle or unthrottle the fan, which leads to different fan powers (at constant rotational speed). However, at a constant rotational speed, the variation of the fan power is within several watts [24]; hence, the change in turbine pressure ratio is small. The turbine characteristics features, therefore, only one point per speed line. The maximum rotational speed of the characteristics was set to 175 krpm, corresponding to the nominal speed for an operation with steam at 220 °C. The turbine was tested up to a temperature of 220 °C corresponding to the design point. Higher temperatures could not be investigated, due to the limitation of the shaft coating (diamond-like carbon), as well as the PTFE o-rings and tubes (maximum temperature of 260 °C). The turbine inlet temperature was maintained with a PID controller connected to the electrical evaporator (Figure 4 (A) at the bottom). Considering the operation with steam, this controller led to mass flow rate fluctuations during a load change, i.e., a higher or lower pump power. Typically, ten up to 60 minutes were necessary to reach a steady operation.

Test procedure: After the startup of the turbine, the turbine was tested consecutively from low to high rotational speeds. The measurement procedure was as follows:

1. Open valve 1 (air) or increase pump power (steam).
2. Wait until the turbine operates steady (only necessary for the operation with steam).
3. Wait until the temperature measurements are steady (up to 90 min). This is overall important for the outlet temperature measurements, e.g., TC5 and TC6.
4. Measure all parameters (sample rate of 1 Hz) for one minute and average the results.

5. Increase the rotational speed and restart at step 1.

These steps were repeated for each of the measured points in Figure 7.

Ambient air (steady): The turbine inlet total temperature was 24 °C and the ambient pressure was 0.96 bar. Pressure ratios between 1.5 to 2.4, mass flow rates between 2.5 kg h⁻¹ and 4.6 kg h⁻¹, respectively, and turbine reactions between 15 % and 20 %, respectively, were measured for rotational speeds between 103 krpm and 175 krpm, respectively.

The measured turbine power 2 and efficiency 2 (∅0.15 mm TC) according to eq. (7) and eq. (9), respectively, was 6.4 W-27.8 W and 28.5 %-32.5 %, respectively. The measured turbine power 1 and efficiency 1 (∅1.5 mm TC) according to eq. (6) and eq. (8), respectively, were consistently lower. As suggested by Krähenbühl [7], the fluid at the turbine outlet rapidly heated up, and thus the measured turbine power was reduced. The difference between power 1 and power 2 was between -3.7 W and -6.3 W. This corresponded to a decrease of the measured power by 58 % and 22.5 %, respectively.

Table 3 lists the temperatures for the nominal operation (175 krpm) with ambient air (top row). The measured corrected total temperature from TC3 (∅0.15 mm) was 1 °C. It was 6 °C lower than the averaged measurement of TC4 and TC5 (∅1.5 mm) and 23 °C lower than the ambient temperature. The bearing temperature close to the turbine was cooler (30 °C) than close to the fan (32 °C) due to the increased heat conduction from the fan to the turbine side.

These temperatures suggest the following heat fluxes: (1) radial and axial heat conduction from the ambient to the outlet measurement section, although it was well insulated with a PTFE tube and glass fiber tapes, (2) heat conduction from the ambient fan side to the turbine, and (3) heat addition by the bearing losses (calculated between 5 W and 16.8 W). A detailed heat loss analysis of this unit by Achi [28] showed, that overall the radial heat loss in the outlet section was significant.

Hot air (steady): During the hot air measurements, the entire test rig was located in an electrical oven (Figure 4). The turbine inlet temperature ranged from 218 °C to 219 °C, which is close to the nominal conditions of 220 °C. The turbine outlet temperature measured with TC4 (∅0.15 mm) ranged from 189 °C to 201 °C and, therefore, was above the oven temperature (180 °C) and the fan inlet temperature (175 °C to 177 °C). The bearing temperature at the turbine side was between 1 °C and 2 °C higher than at the fan side. These temperature levels suggest three heat conduction effects: (1) from the outlet test section in axial direction to the ambient (25 °C), (2) from the outlet test section in radial direction to the oven, and (3) from the turbine to the fan side. In comparison to the ambient air case, the heat fluxes are inversed.

The measured power 1 and efficiency 1 (∅1.5 mm TC) was, therefore, consistently higher than power 2 and efficiency 2 (∅0.15 mm TC). The difference between the measured power 1 and power 2 decreased from 4 W (110 krpm) to 2.9 W (175 krpm). Similarly, the difference between efficiency 1 and efficiency 2 decreased from 11 % points to 2.9 % points. Table 3 in the middle lists the temperatures for the nominal point. Here, the turbine outlet temperature (189 °C) is closer to the oven temperature and closer to the fan inlet temperature (176 °C). As a result of the reduced temperature gradients, the heat conduction was reduced and the two power and efficiency

definitions showed less deviations.

The reduced mass flow rate of the hot air was slightly below the ambient air case. This resulted from the reduced heat capacity ratio (κ), which is 1.39 for hot air and 1.40 for ambient air. The theoretical value of the reduced mass flow rate ratio of hot air to ambient air is 0.994 ($\sqrt{\frac{1.39}{1.40}}$). The measured values ranged from 0.987 and 0.990, indicating a good repeatability of the mass flow rate measurement device.

The turbine reaction was decreased by 3 % points (at 110 krpm) up to 4.4 % points (at 175 krpm), since the turbine was operated closer to its design conditions. At 220 °C, the velocity of sound of hot air and water vapor is 444 ms⁻¹ and 543 ms⁻¹, respectively. Thus, the rotor losses were reduced, although the Reynolds number based on the hydraulic diameter of the throat section ($Re_{d_{hyd}}$) was reduced from 3.0×10^4 to 1.6×10^4 . A lower Reynolds number leads to increased frictional losses in the turbine channels.

At the nominal rotation speed of 175 krpm, the turbine operated with a pressure ratio of 2.4, a mass flow rate of 3.5 kg h⁻¹, a reaction of 0.16, yielding a power of 32 W at an efficiency of 29 %.

Water vapor (SOFC, steady): Figure 7 also shows the experimental results of the steam turbine by Wagner et al. [15] for an operation in the relevant environment (6 kW_e SOFC). The reduced steam mass flow rate is lower than that of ambient and hot air. Compared to air, steam has a higher gas constant ($R_{g,WV} = 461 \text{ J kg}^{-1} \text{ K}^{-1}$) and a lower heat capacity ratio ($\kappa_{WV} = 1.32$). The measured ratio of the reduced mass flow rate of water vapor to hot air is between 0.73 ± 0.06 at 115 krpm and up to 0.77 ± 0.08 at 170 krpm. Assuming similar inlet temperatures and pressures and neglecting the slightly different Mach numbers in the throat, the analytical value is 0.77 ($\sqrt{\frac{R_{g,HA} \kappa_{WV}}{R_{g,WV} \kappa_{HA}}} = \sqrt{\frac{287 \cdot 1.322}{461 \cdot 1.39}}$). Although the measurement uncertainty of the pump is relatively high ($\pm 2 \text{ kg h}^{-1} \sqrt{\text{K bar}^{-1}}$), the two measurements correlate.

Considering similar pressure ratios, the turbine reaction is slightly reduced, suggesting lower rotor losses, due to (1) a slightly higher Reynolds number $Re_{d_{hyd}}$ (2×10^4 instead of 1.6×10^4) and (2) an operation close to the nominal point. Reactions between 12.3 % (at 115 krpm) and up to 13.8 % (at 170 krpm) were measured.

Comparison to CFD: Considering the operation with steam, Wagner et al. [15] reported isentropic efficiencies between 42 % at 115 krpm and 30 % at 170 krpm. These measurements are clearly influenced by heat conduction, since the efficiency should increase towards the nominal point (175 krpm). The corrected efficiency according to eq. (12) is more feasible, since it increases from 38 % to 40 % with increasing pressure ratio. This correlates within ± 7 % to the value of the CFD simulations, which increases from 36 % to 43 %. The corrected power according to eq. (13) varied between 13 W and 28 W and is 9 % to 15 % higher than the value of the CFD simulation.

A similar trend of decreasing isentropic efficiencies with increasing pressure ratio is observed for the hot air case. Efficiency 1 ($\varnothing 1.5 \text{ mm}$) decreases from 46 % to 32 %, efficiency 2 ($\varnothing 0.15 \text{ mm}$) decreases less significant from 34 % to 29 %, and the corrected efficiency 2 from 46 % to 43 %, whereas the simulated efficiency increases from 40 % to 45 %.

The CFD simulation overestimates the actual turbine performance, since several loss effects are neglected: (1) partial admission losses

(single passage simulation), (2) surface roughness (smooth walls), and (3) heat conduction (adiabatic walls). Additionally, the turbine features increased losses in off-design operation, and thus the steady simulation is limited in accuracy. The corrected efficiency overestimates the actual turbine efficiency, if heat is conducted to the fan fluid domain. This heat addition leads to an underestimation of the fan isentropic fan efficiency [24], and thus to an overestimation of the corrected turbine efficiency according to eq. (12). Considering the operational point at 175 krpm with hot air, the authors suggest that the CFD simulation (45 %) and the corrected efficiency 2 (43 %) overestimate the actual turbine efficiency, whereas the efficiency 2 (29 %) underestimates it. A similar conclusion is drawn for the ambient air case: the actual turbine efficiency is expected above 33 % (efficiency 2), but below 47 % (CFD simulation).

Compared to the measurements, the simulated mass flow rate is underestimated by 16 % and 20 % for ambient and hot air, respectively. The authors exclude a leakage at the non-admission part of the turbine, since it was sealed with a PTFE o-ring (Figure 2). The measurement uncertainty (less than $\pm 0.2 \text{ kg h}^{-1} \sqrt{\text{K bar}^{-1}}$) is also too low to explain this deviation. However, the manufacturing tolerances have a significant impact, e.g., a smaller stator blade TE thickness (t_6) or a higher blade angle ($\alpha_{6,blade}$). The effective stator height is higher than 0.7 mm due to the milling tool traces at the stator hub (Figure 2 on the left). Considering the operation with water vapor, the simulated points at 115 krpm, 131 krpm, and 150 krpm are within the pump measurement uncertainty ($\pm 2 \text{ kg h}^{-1} \sqrt{\text{K bar}^{-1}}$).

The simulated degree of reactions for hot air, and water vapor show the same trend as the measured ones. However, the simulated reactions are between 20 % to 43 % higher. The turbine rotor-stator pressure tap is relatively big ($\varnothing 0.15 \text{ mm} = 2t_6$) and located at a highly transient region. Thus, a comparable data extraction from the steady CFD simulation is challenging.

Water vapor (NP, steady): The turbine was characterized at its nominal point with water vapor at 175 krpm at an oven temperature, similar to the hot air tests (180 °C), using solely the $\varnothing 1.5 \text{ mm}$ thermocouples (leakage and mechanical constraints on the $\varnothing 0.15 \text{ mm}$ ones). The accurate measurement of the turbine isentropic efficiency is simplified, due to the reduced viscosity of water vapor and the resulting reduced windage losses: the estimated bearing losses are lower (12 W), compared to the hot air case (19 W), as listed in Table 3. Additionally, the heat conduction effects were minimized, by adjusting the temperature levels as indicated in Table 3: The turbine inlet temperature (211 °C) decreased to 182 °C and the fan inlet temperature (157 °C) increased to 181 °C. Hence, both outlet temperatures were slightly above the oven temperature (180 °C), leading to decreased heat conduction. Additionally, the fan flow was the major heat sink for the bearing losses. The actual turbine efficiency is expected between the uncorrected efficiency 1 (37 %) and the corrected efficiency 1 (42 %). This correlates to the analytical models of Balje and Soderberg (40 %) and the steady single passage CFD predictions (41 %), listed in Table 4. It also lists the result of the transient CFD simulation, which is comparable to the steady one. The turbine reaction of 18 % simulated with the unsteady simulation is closer to the experimental result (15 %). At this nominal point, the measured pressure ratio was 2.0 and the mass flow rate was 2.3 kg h^{-1} , resulting in a turbine power between 34 W and 38 W.

COMPARISON OF THE EXPERIMENTAL RESULTS TOWARDS ANALYTICAL MODELS

For efficient turbine design, zero and one-dimensional models are essential to obtain an accurate baseline geometry. The calculations presented in this section are based on the previous water vapor measurements ($p_{t,4} = 2 \text{ bar}$, $T_{t,4} = 211^\circ\text{C}$, $p_{amb} = 0.97 \text{ bar}$, $\dot{m}_1 = 2.3 \text{ kg h}^{-1}$, and $n_{rot} = 175 \text{ krpm}$).

Zero-dimensional model: The specific speed in eq. (4) and the specific diameter

$$d_s = d_7 \frac{\Delta h_{is,tst}^{0.25}}{\sqrt{\dot{V}_8}} \quad (16)$$

are 0.09 and 8, respectively, using the angular speed (ω), the volume flow rate at the rotor TE (\dot{V}_8), the total-to-static isentropic specific enthalpy difference ($\Delta h_{is,tst}$), and the turbine tip diameter (d_7). According to the similarity concepts by Balje [17] (figure 5.44 for partial-admission turbines with low reaction), the total-to-static isentropic efficiency is predicted to 63.5%. However, this efficiency corresponds to a machine operated at a relative tip clearance of 0.02, but it is 0.244 for the actual manufactured and tested turbine. For higher relative tip clearances Balje suggests a correction factor of 0.72 ($1.025 - \frac{0.10}{0.08} 0.244$, figure 5.31 based on $n_s = 0.08$), resulting in a corrected isentropic efficiency of 45.7%. Additional losses occur due to the high TE and LE to blade height ratio of 0.15. Balje suggests a correction of 0.87 ($1.02 - 1 \cdot 0.15$, figure 5.32 based on $n_s = 0.08$) for thick blade edges, which results in an isentropic efficiency of 39.8%, that is on the order of the experimental value of 37.3% (Table 4).

One-dimensional model: Soderberg [18] describes a loss correlation for turbines at optimal load coefficient according to the Zweifel criterion [29] at zero incidence, a Reynolds number based on the hydraulic diameter of the rotor TE throat section ($Re_{d_{hyd}}$) of 10^5 , an aspect ratio defined with the blade height and the radial blade chord ($\frac{H}{r_7 - r_8}$) of three, a maximum blade thickness to radial chord ratio ($\frac{t_{max}}{r_7 - r_8}$) of 0.2, and a deflection lower than 120° . The “nominal” loss coefficient,

$$\zeta = 0.04 + 0.06 \left(\frac{\frac{\pi}{2} - \alpha_7 + \frac{\pi}{2} - \alpha_8}{\pi \frac{100}{180}} \right)^2 \quad (17)$$

is a function of the blade deflection. If the aspect ratio or the Reynolds number differ from the conditions above, Soderberg provides a correlation to adapt the nominal loss coefficient for both rotor

$$\zeta_{stator} = \left((1 + \zeta) \left(0.993 + 0.021 \frac{r_7 - r_8}{H} \right) - 1 \right) \left(\frac{10^5}{Re_{d_{hyd}}} \right)^{0.25} \quad (18)$$

and stator.

$$\zeta_{rotor} = \left((1 + \zeta) \left(0.975 + 0.075 \frac{r_7 - r_8}{H} \right) - 1 \right) \left(\frac{10^5}{Re_{d_{hyd}}} \right)^{0.25} \quad (19)$$

The Reynolds number ($Re_{d_{hyd}}$) definition is based on the rotor TE: the absolute velocity (c_8) and the hydraulic diameter

$$d_{hyd,8} = \frac{2 \frac{\pi d_8}{z_{rotor}} \cos \beta_{8,blade} H_8}{\frac{\pi d_8}{z_{rotor}} \cos \beta_{8,blade} + H_8} \quad (20)$$

which is based on the channel depth ($\frac{\pi d_8}{z_{rotor}} \cos \beta_{8,blade}$) and the rotor blade height (H_8). The total-to-static isentropic efficiency is thus a function of eq. (18) and eq. (19), as well as the turbine total-to-total specific enthalpy difference (Δh_{tt}).

$$\eta_{is,st} = \frac{1}{1 + \frac{1}{2\Delta h_{tt}} (\zeta_{rotor} w_8^2 + \zeta_{stator} c_7^2 + c_8^2)} \quad (21)$$

Since the conditions at the turbine rotor TE (turbine section 8) are not known a priori, an iterative procedure is necessary as detailed in the Appendix. Equation (21) suggests an efficiency of 40.0 % at the nominal point, indicating good accuracy (Table 4).

Therefore, the authors conclude that the zero-dimensional similarity concepts by Balje [17] with the blade tip clearance and blade edge corrections and the one-dimensional loss correlations by Soderberg [18] with Reynolds number and blade height corrections are both viable for this specific micro steam turbine. However, the turbine discharge coefficient (CD) has to be estimated a priori. The CD value was 0.86 for the experiment at the nominal point with steam.

CONCLUSION

An extensive literature review demonstrated a lack of: (1) Experimental realization and characterization of micro steam turbines, (2) reliable test procedures to measure power and efficiency of micro turbines based on inlet and outlet enthalpies, and (3) validations of simple zero- and one-dimensional models for micro turbines. All three aspects were addressed in this paper:

(1) A micro steam turbine with a tip diameter of 15 mm was designed and experimentally characterized. The steam turbine is conceived as a radial-inflow, low-reaction (15 %), and partial admission (21 %) machine with 59 blades (blade height of 0.6 mm and radial chord length of 1 mm). At the nominal mass flow rate and total-to-static pressure ratio of 2.3 kg h^{-1} and 2, respectively, the turbine yielded a measured power of 34 W and a total-to-static isentropic efficiency of 37 %. Steady and transient single passage CFD simulation showed

good agreement with the measurements.

(2) A conventional measurement setup with $\varnothing 1.5$ mm thermocouples (installed at 135-times and 80-times the blade radial chord length of 1 mm downstream and upstream of the rotor, respectively) was compared to a novel setup with $\varnothing 0.15$ mm thermocouples (installed 3-times and 8-times downstream and upstream, respectively). The most-accurate measurements were obtained, if the turbine inlet temperature was adjusted in such way, that the turbine outlet temperature corresponded to the surrounding temperature. Additionally, a heat sink for the bearing losses (35 % of the turbine power at nominal conditions) can further enhance the experimental measurements. The measurement setup for water vapor was found to be more accurate than for the hot air setup, due to: (1) the lower viscosity of water vapor, and thus reduced bearing losses, (2) the higher heat capacity of steam, and thus higher capacity to heat the outlet side test section, and (3) the nominal operation of the turbine rotor for the case with steam, and thus reduced losses.

(3) Zero-dimensional similarity concepts by Balje with blade tip clearance and blade edge corrections and one-dimensional loss correlations by Soderberg with Reynolds number and blade height corrections, both showed accurate efficiency predictions (40 %) with respects to the measurements (37 %) and the steady single passage CFD simulation (41 %). The authors, therefore, conclude, that the pre-design correlations by Balje, as well as the mean-line model by Soderberg and the CFD simulation, are valid for this specific micro steam turbine design procedure and simulation at the nominal conditions, respectively.

ACKNOWLEDGMENT

The authors acknowledge Marcos Font [22] and Diya Achi [28], the research grant from the Canton de Vaud under the “100 million de francs pour les energies renouvelables et l’efficacite energetique” program, and the Horizon 2020 Research and Innovation Programme under Grant Agreement No. 815284.

REFERENCES

- [1] Epstein, A. H., 2004. “Millimeter-Scale, Micro-Electro-Mechanical Systems Gas Turbine Engines”. *Journal of Engineering for Gas Turbines and Power*, **126**(2), Apr., pp. 205–226.
- [2] Kang, S., Johnston, J. P., Arima, T., Matsunaga, M., Tsuru, H., and Printz, F. B., 2004. “Microscale Radial-Flow Compressor Impeller Made of Silicon Nitride: Manufacturing and Performance”. *Journal of Engineering for Gas Turbines and Power*, **126**(2), Apr., pp. 358–365.
- [3] Tanaka, S., Hikichi, K., Togo, S., Murayama, M., Hirose, Y., Sakurai, T., Yuasa, S., Teramoto, S., Niino, T., Mori, T., Esashi, M., and Isomura, K., 2007. “World’s smallest gas turbine establishing brayton cycle”. *7th International Workshop on Micro and Nanotechnology for Power Generation and Energy Conversion Applications (PowerMEMS 2007)*, 01.
- [4] IHI Cooperation, 2012. 世界初の携行型超小型ガスタービン発電機を開発. https://www.ihico.jp/ihico/all_news/2011/aeroengine_space_defense/2012-2-16/index.html. Accessed: 2019-11-04.

- [5] Peirs, J., Reynaerts, D., and Verplaetsen, F., 2003. “Development of an axial microturbine for a portable gas turbine generator”. *Journal of Micromechanics and Microengineering*, **13**(4), June, pp. S190–S195.
- [6] Arnold, D. P., Galle, P., Herrault, F., Das, S., Lang, J. H., and Allen, M. G., 2005. A Self-Contained, Flow-Powered Microgenerator System. Tech. rep., Georgia Tech.
- [7] Krahenbuhl, D., Zwysig, C., Horler, H., and Kolar, J. W., 2008. “Design Considerations and Experimental Results of a 60 W Compressed-Air-to-Electric-Power System”. In 2008 IEEE/ASME International Conference on Mechatronic and Embedded Systems and Applications, pp. 375–380.
- [8] Krahenbuhl, D., Zwysig, C., Weser, H., and Kolar, J. W., 2009. “Theoretical and experimental results of a mesoscale electric power generation system from pressurized gas flow”. *Journal of Micromechanics and Microengineering*, **19**(9), Aug., p. 094009.
- [9] Sato, S., Jovanovic, S., Lang, J., and Spakovszky, Z., 2011. “Demonstration of a Palm-Sized 30 W Air-to-Power Turbine Generator”. *Journal of Engineering for Gas Turbines and Power*, **133**(10), May, pp. 102301–102311.
- [10] Fu, L., Feng, Z., and Li, G., 2017. “Experimental investigation on overall performance of a millimeter-scale radial turbine for micro gas turbine”. *Energy*, **134**, Sept., pp. 1–9.
- [11] Paulides, J., Post, E., Post, J., Encica, L., and Lomonova, E., 2015. “Green turbine: A high speed double turbine solution for sustainable energy harvesting from waste heat”. In 2015 Tenth International Conference on Ecological Vehicles and Renewable Energies (EVER), IEEE, pp. 1–7.
- [12] Kim, C. K., and Yoon, J. Y., 2016. “Performance analysis of bladeless jet propulsion micro-steam turbine for micro-CHP (combined heat and power) systems utilizing low-grade heat sources”. *Energy*, **101**, Apr., pp. 411–420.
- [13] Placco, G. M., and Guimarães, L. N. F., 2020. “Power Analysis on a 70-mm Rotor Tesla Turbine”. *Journal of Energy Resources Technology*, **142**(3), Mar.
- [14] Wagner, P. H., Wuillemin, Z., Diethelm, S., Van herle, J., and Schiffmann, J., 2017. “Modeling and Designing of a Radial Anode Off-Gas Recirculation Fan for Solid Oxide Fuel Cell Systems”. *Journal of Electrochemical Energy Conversion and Storage*, **14**(1), May.
- [15] Wagner, P. H., Wuillemin, Z., Constantin, D., Diethelm, S., Van herle, J., and Schiffmann, J., 2020. “Experimental characterization of a solid oxide fuel cell coupled to a steam-driven micro anode off-gas recirculation fan”. *Applied Energy*, **262**, Mar., p. 114219.
- [16] Jovanovic, S., 2008. “Design of a 50-watt air supplied turbogenerator”. Master’s thesis, MIT.
- [17] Balje, O. E., 1981. *Turbomachines : a guide to design, selection and theory*. Wiley, New York etc.
- [18] Soderberg, C., 1949. Unpublished notes, Gas Turbine Laboratory, MIT.
- [19] Glassman, A. J., 1994. Turbine design and application volumes 1, 2, and 3. Tech. rep., June.
- [20] Stenning, A. H., 1953. Design of turbines for high-energy-fuel low-power-output applications. Tech. rep. Report number 79, Department of Mechanical Engineering, MIT, Sept.

- [21] R. I. Lewis, 1996. *Turbomachinery performance analysis*. Arnold, London.
- [22] Font, A. M., 2019. “Analytical and numerical investigation of a small-scale radial-inflow turbine”. Master’s thesis, EPFL, Lausanne. <https://upcommons.upc.edu/handle/2117/134806>. Accessed: 2019-11-19.
- [23] Dunavant, J. C., and Erwin, J. R., 1956. Investigation of a related series of turbine-blade profiles in cascade. Tech. rep., Oct.
- [24] Wagner, P. H., Van herle, J., and Schiffmann, J., 2020. “Theoretical and Experimental Investigation of a Small-Scale, High-Speed, and Oil-Free Radial Anode Off-Gas Recirculation Fan for Solid Oxide Fuel Cell Systems”. *Journal of Engineering for Gas Turbines and Power*, **142**(4), Apr.
- [25] Hirschberg, A., and Van Muiswinkel, J., 1977. “A correlation of recovery temperature data for cylinders in a compressible flow at high reynolds numbers”. *International Journal of Heat and Mass Transfer*, **20**(6), June, pp. 669–674.
- [26] Demierre, J., Rubino, A., and Schiffmann, J., 2014. “Modeling and Experimental Investigation of an Oil-Free Microcompressor-Turbine Unit for an Organic Rankine Cycle Driven Heat Pump”. *Journal of Engineering for Gas Turbines and Power*, **137**(3), Oct.
- [27] Menter, F. R., 1993. “Zonal Two Equation Kappa-Omega Turbulence Models for Aerodynamic Flows”.
- [28] Achi, D., 2020. “Experimental and Numerical Investigation of a Small-Scale Steam Turbine”. Semester project, EPFL, Lausanne. <https://infoscience.epfl.ch/record/276092> Accessed: 2020-03-06.
- [29] Zweifel, O., 1945. The spacing of turbomachine blading, especially with large angular deflection. *Brown Boveri Review*, 32, 12.

APPENDIX

The similarity concepts by Balje [17] and the loss model by Soderberg [18] are based on the turbine geometrical parameters (Table 2), as well as the measured inlet conditions (\dot{m}_1 , $p_{t,4}$, and $T_{t,4}$), outlet conditions ($p_{st,9}$, p_{amb}), and rotational speed (n_{rot}) for the nominal conditions with water vapor. The former uses the volume flow rate at the rotor TE ($\dot{V}_8 = \frac{\dot{m}_1}{\rho_8}$) and the latter uses the relative and absolute velocity at the rotor TE (w_8 and c_8 , respectively). These variables are based on the rotor TE density (ρ_8), which is not known a priori. Therefore, an iterative procedure is necessary, as illustrated in the following Nassi-Shneiderman diagram in Figure 8. The mean-line analysis is used, assuming a deviation of zero at the stator and rotor TE.

TABLE 1. OVERVIEW OF MICRO TURBINES DRIVEN BY AMBIENT AIR (TOP) AND STEAM (BOTTOM) AT TEMPERATURES BETWEEN 150 °C AND 220 °C. NON-FORMATTED NUMBERS ARE DIRECTLY STATED IN THE REFERENCE (MEASUREMENTS), **BOLD** AND UNDERLINED INFORMATION WAS CALCULATED AND ESTIMATED, RESPECTIVELY, BY THE AUTHORS OF THIS PAPER WITH THE DATA AVAILABLE IN THE REFERENCE. A DASH (-) INDICATES THAT NO DATA WAS GIVEN IN THE REFERENCE.

Year of Ref.	Authors or Company	Tip diam. in mm	Rot. speed in krpm	Efficiency in %	Power in Watt	Bearing type ^c	Turbine type	Power meas. method ^g	Ref.
Ambient air									
2003	Peirs et al.	9.9	100	18 ^a	28 ^c	BB	axial impulse	EM	[5]
2005	Arnold et al.	10	200	8^b	1.1 ^d	BB	dental drill	EM	[6]
2008	Krähenbühl et al.	9.5	370	28 ^a	143^c	BB	axial impulse	EM&HT	[7]
2009	Krähenbühl et al.	10.5	495	52 ^a	206^c	BB	radial-inflow	EM	[8]
2011	Sato et al.	10	360	47 ^a	37^c	BB	radial-inflow	EM	[9]
2017	Fu et al.	10.6	360	58 ^a	<u>96^c</u>	Static GB	radial-inflow	HC	[10]
2020	Wagner et al. ^f	15	175	33 ^a	28 ^c	Dyn. GB	radial-inflow	HT	
Steam									
2015	Green turbine	-	30	44^b	1400 ^d	BB	axial impulse	EM	[11]
2016	Kim et al.	144	27.8	19.7 ^a	4650 ^c	BB	Hero	EM	[12]
2020	Placco et al.	70	1.3	25 ^a	18 ^c	BB	Tesla	DM	[13]
2020	Wagner et al. ^f	15	175	37 ^a	34 ^c	Dyn. GB	radial-inflow	HT	

^a Total-to-static isentropic efficiency ^b Overall efficiency (ratio of electrical power to turbine isentropic power)

^c Turbine shaft power ^d Electrical power of generator (shaft power not indicated) ^e The bearing type: ball bearings (BB), static gas film bearing (static GB), and dynamic gas film bearing (dyn GB) ^f Results are extracted from Figure 7

^g Turbine power was measured with: (EM) electrical motor power and estimated electrical motor and mechanical efficiency, (HC) inlet and outlet flow enthalpies of load compressor or (HT) turbine, and (DM) dynamometer

TABLE 2. GEOMETRICAL TURBINE PARAMETERS: (A) VOLUTE AND INDUCER, (B) STATOR, (C) ROTOR, AND (D) AXIAL AND RADIAL CLEARANCES. THE BLADE ANGLES ARE DEFINED WITH RESPECT TO THE CIRCUMFERENTIAL DIRECTION IN DEGREE AND ALL DIMENSIONS ARE GIVEN IN mm. THE TURBINE SECTIONS AND PARAMETERS ARE DEFINED IN FIGURE 2, 3, and 4 (C).

(A)	(B)	(C)	(D)
Volute (tunnel-type, 3.1-4)	Turbine stator (5-6)	Turbine rotor (7-8)	Axial clearances (S) (from zero to nominal speed)
Tunnel type volute inlet (3.1) $R_{3,1}$ 2 $b_{3,1}$ 0.7	Stator leading edge (5) $\alpha_{5,blade}$ 43.7 t_5 0.25	Rotor leading edge (7) $\beta_{7,blade}$ 143.7 t_7 0.09	Blade tip clearance S_{tip} 0.133 to 0.143
Tunnel type volute outlet (3.2) $R_{3,2}$ 0.56 $b_{3,2}$ 0.7	r_5 8.65 $H_5 = b_5$ 0.70	r_7 7.50 H_7 0.586	Turbine backface clearance S_{back} 0.115 to 0.105
Turbine inducer (4-5)	Stator trailing edge (6) $\alpha_{6,blade}$ 22 t_6 0.08	Rotor trailing edge (8) $\beta_{8,blade}$ 41.7 t_8 0.08	Turbine hub and stator hub (reference) axial offset (S) S_{offset} -0.019 to -0.029
Inducer inlet (4) r_4 13 b_4 0.7	r_6 7.65 $H_6 = b_6$ 0.70	r_8 6.50 H_8 0.586	Radial clearances (S)
	Stagger angle 58.6	Stagger angle 6.6	Rotor-stator Seal S_{radial} 0.125 S_{seal} 0.125
	Chord 1.92 Chamber 1.93	Chord 1.01 Chamber 1.24	
	z_{stator} 12 (out of 61)	z_{rotor} 59	
	Admission of $\frac{12+1}{61} = 0.213$	Channel width (b) $b_7 = b_8 = 0.7 - S_{offset}$	

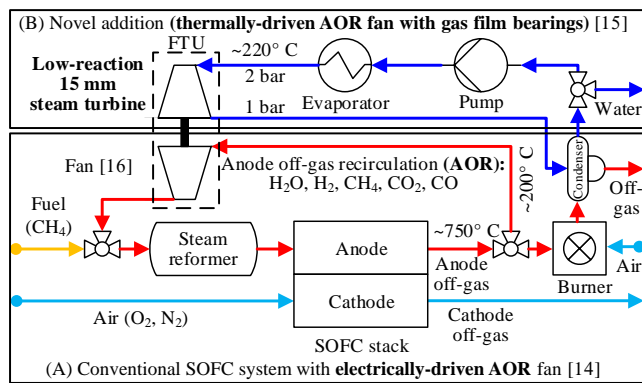
TABLE 3. CORRECTED TOTAL TEMPERATURES (LEFT) AND ESTIMATED MECHANICAL POWER LOSS OF THE SHAFT AND ROTOR (RIGHT) FOR THE NOMINAL OPERATION POINT AT 175 krpm FOR DIFFERENT FLUIDS: AMBIENT AIR, HOT AIR, AND WATER VAPOR. FOR THE FIRST CASE, THE MAIN HEAT FLUX IS FROM THE FAN TO THE TURBINE, AND VICE VERSA FOR THE LAST TWO CASES.

Corrected total temperatures in °C at 175 krpm	In (TC2) $\varnothing 1.5$ mm	Turbine		Bearing side		Fan In	Oven	Bearing mech. loss in W
		Out (TC3 and TC4-5) $\varnothing 0.15$ mm	$\varnothing 1.5$ mm	Turbine	Fan			
Ambient air (AA)	24	1	7	30	32	24	24	16.8
Hot air (HA)	219	189	184	203	201	176	180	19.3
Water vapor (WV)	211	-	182	191	189	157	180	11.8

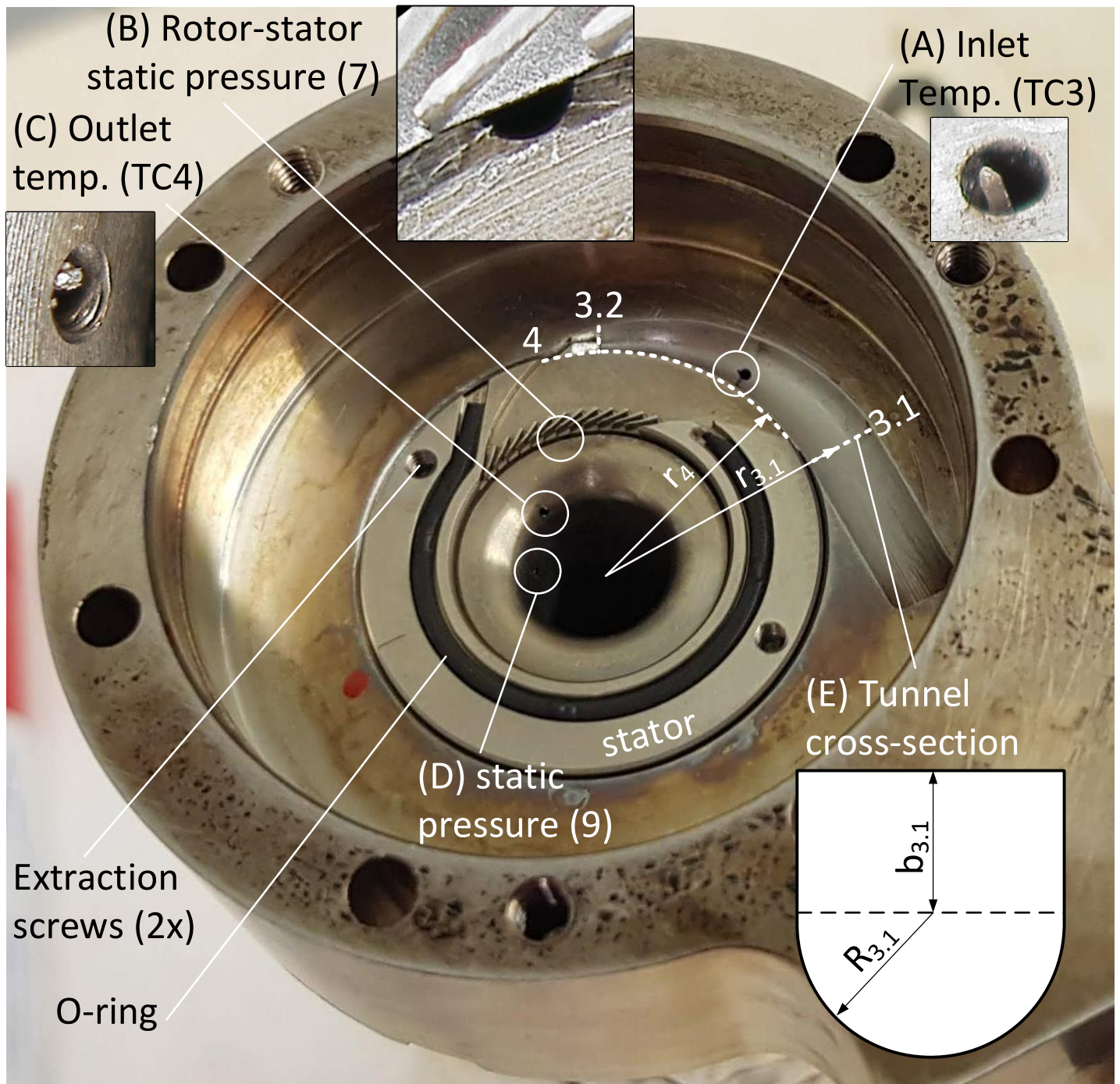
TABLE 4. COMPARISON OF THE NOMINAL STEAM TURBINE CHARACTERISTIC (MASS FLOW RATE, REACTION, POWER, AND TOTAL-TO-STATIC ISENTROPIC EFFICIENCY), DETERMINED WITH AN EXPERIMENT, WITH ZERO-DIMENSIONAL SIMILARITY CONCEPTS BY BALJE, WITH ONE-DIMENSIONAL LOSS CORRELATIONS BY SODERBERG, AND WITH A SINGLE PASSAGE (SP) STEADY AND TRANSIENT CFD SIMULATION. THE TOTAL INLET TEMPERATURE IS 211 °C, THE TOTAL-TO-STATIC PRESSURE RATIO IS 2, THE AMBIENT PRESSURE IS 0.97 bar, AND THE ROTATIONAL SPEED IS 175 krpm (BLUE DOWN-POINTING TRIANGLE IN FIGURE 7).

Nominal point	Mass flow rate in kg h⁻¹	Reaction	Power in W	Eff. in %
Exp.	2.28	0.15	33.5	37.3
Exp. (corrected)	2.28	0.15	37.8	42.0
Balje [17]	2.28 ^a	-	35.7	39.8
Soderberg [18]	2.28 ^a	-	35.5	40.0
SP CFD (steady)	1.92	0.22	31.2	41.1
SP CFD (trans.)	1.93	0.18 ^b	31.2 ^c	41.0

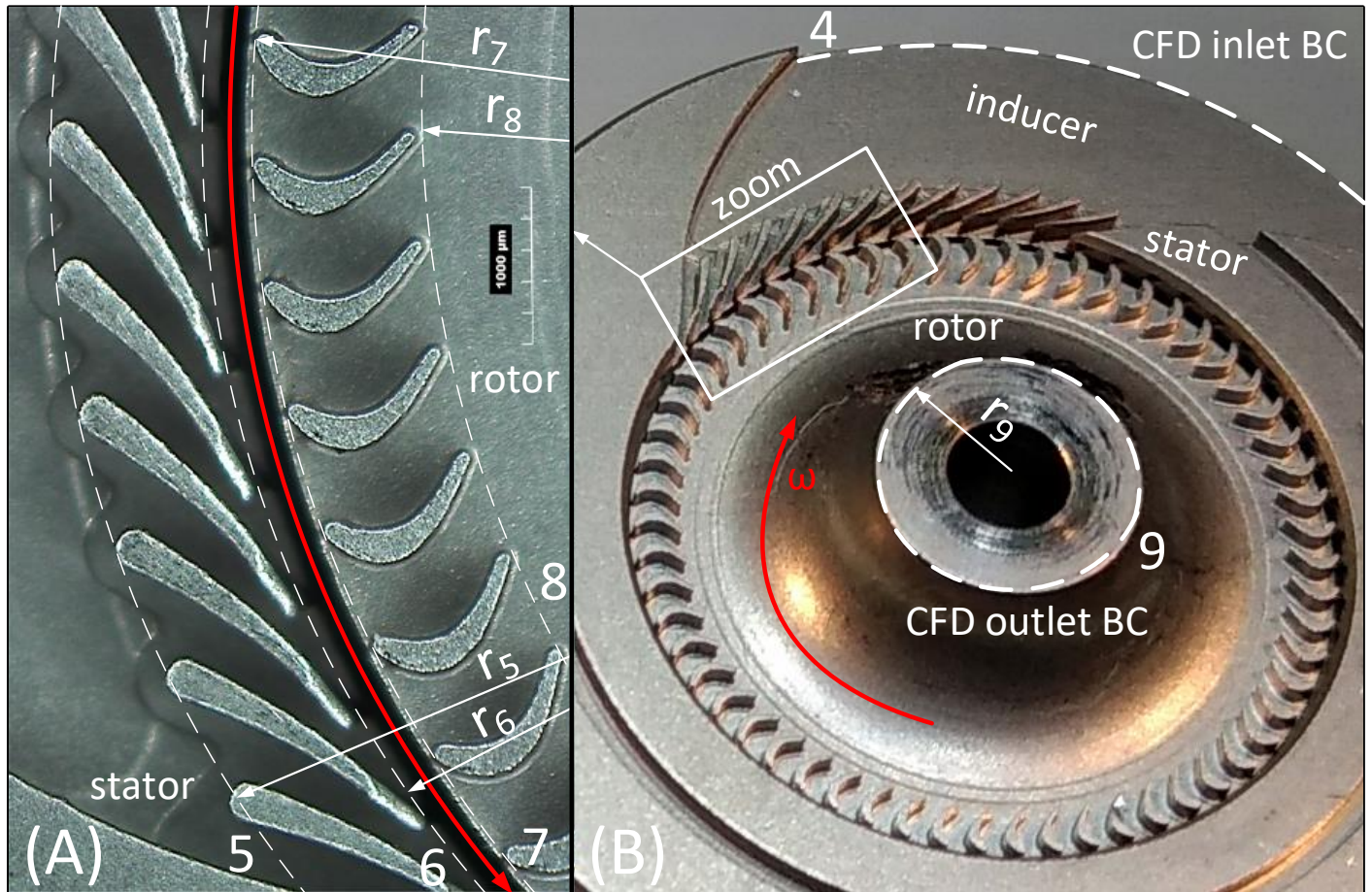
^a The measured discharge coefficient ($CD = 0.86$) was assumed, which might not be known a-priori ^b Averaged value over one blade passing period (0.165 to 0.205) ^c Averaged value over one blade passing period (28.4 W to 34.3 W)



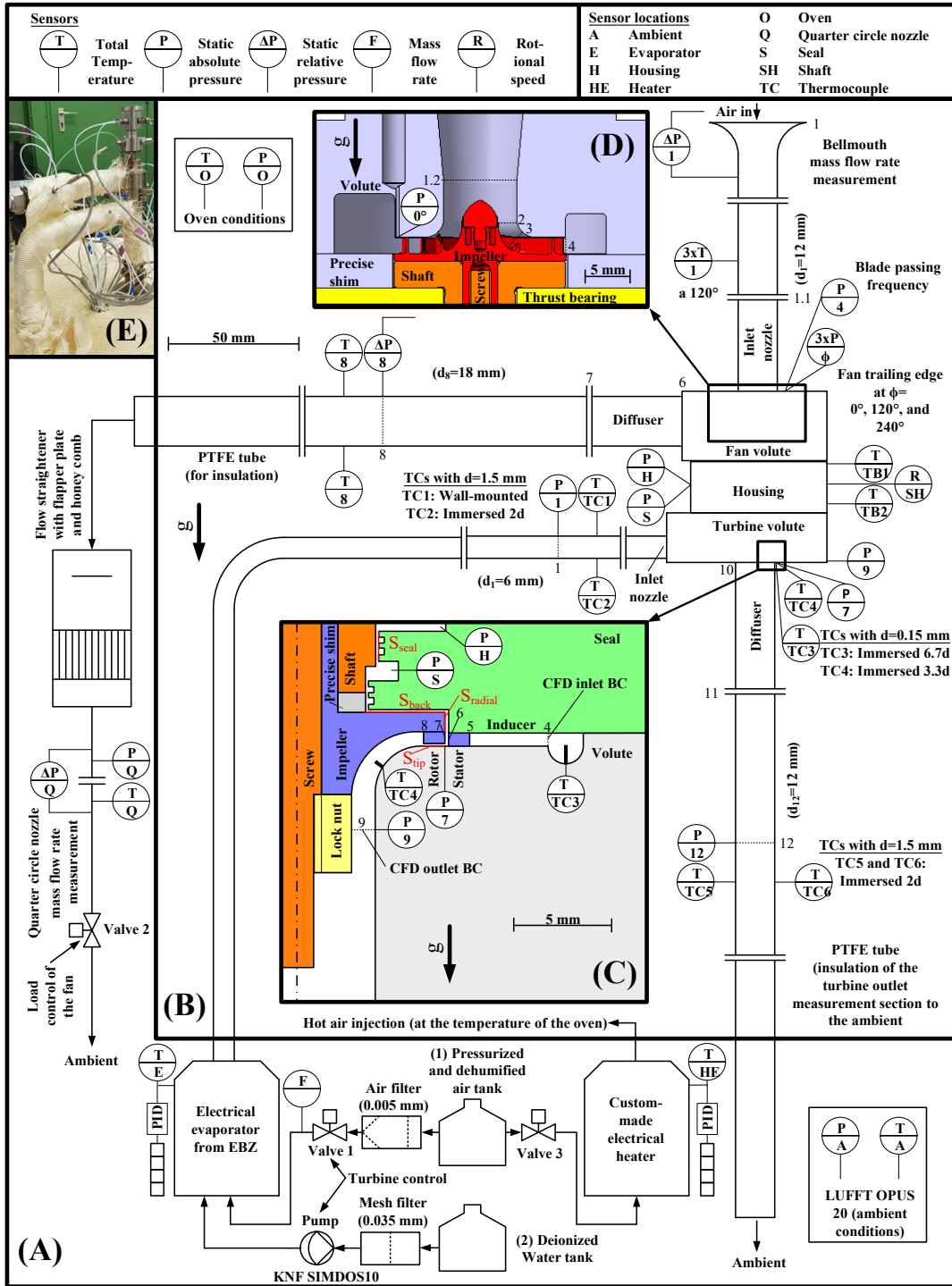
GTP-20-1474-FIGURE 1. FLOW SHEET OF (A) A CONVENTIONAL SOFC SYSTEM WITH AN ELECTRICALLY-DRIVEN AOR FAN AND (B) WITH A THERMALLY-DRIVEN AOR FAN, THE FAN-TURBINE UNIT. (ADAPTED FROM [24])



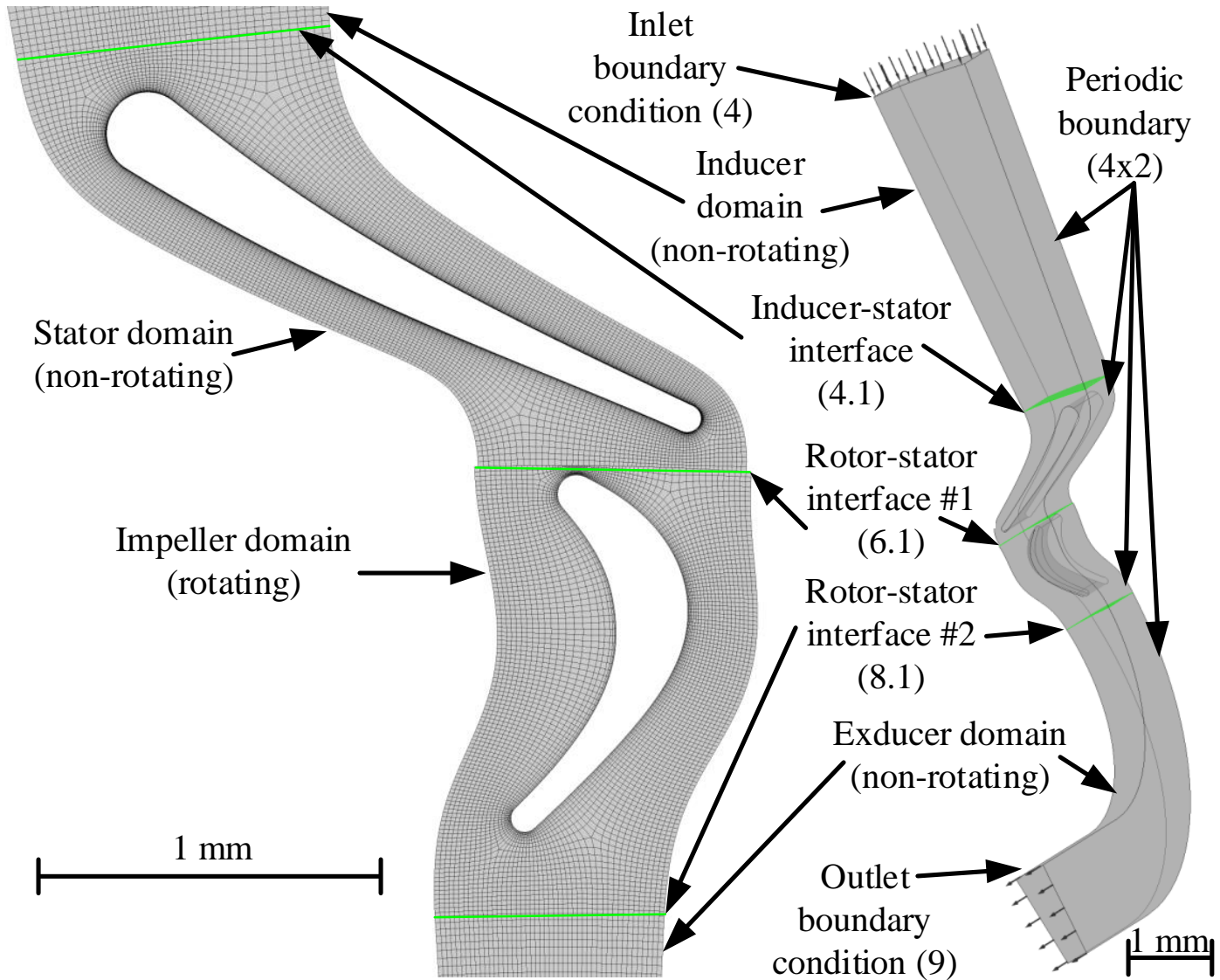
GTP-20-1474-FIGURE 2. THE MANUFACTURED PARTIAL-ADMISSION TURBINE VOLUTE AFTER TESTS WITH STEAM AT 220 °C, THE REMOVABLE TURBINE STATOR, (A) THE TEMPERATURE MEASUREMENT AT THE VOLUTE WITH A $\varnothing 0.15$ mm THERMOCOUPLE, (B) THE HALF CIRCLE STATIC PRESSURE MEASUREMENT TAP ($\varnothing 0.15$ mm) AT THE ROTOR-STATOR INTERFACE, (C) THE (BROKEN) $\varnothing 0.15$ mm THERMOCOUPLE DOWNSTREAM OF THE TURBINE TE, (D) THE STATIC PRESSURE MEASUREMENT CLOSE TO THE CFD OUTLET BOUNDARY CONDITION, AND (E) THE DIMENSIONS OF THE TUNNEL CROSS-SECTION VOLUTE.



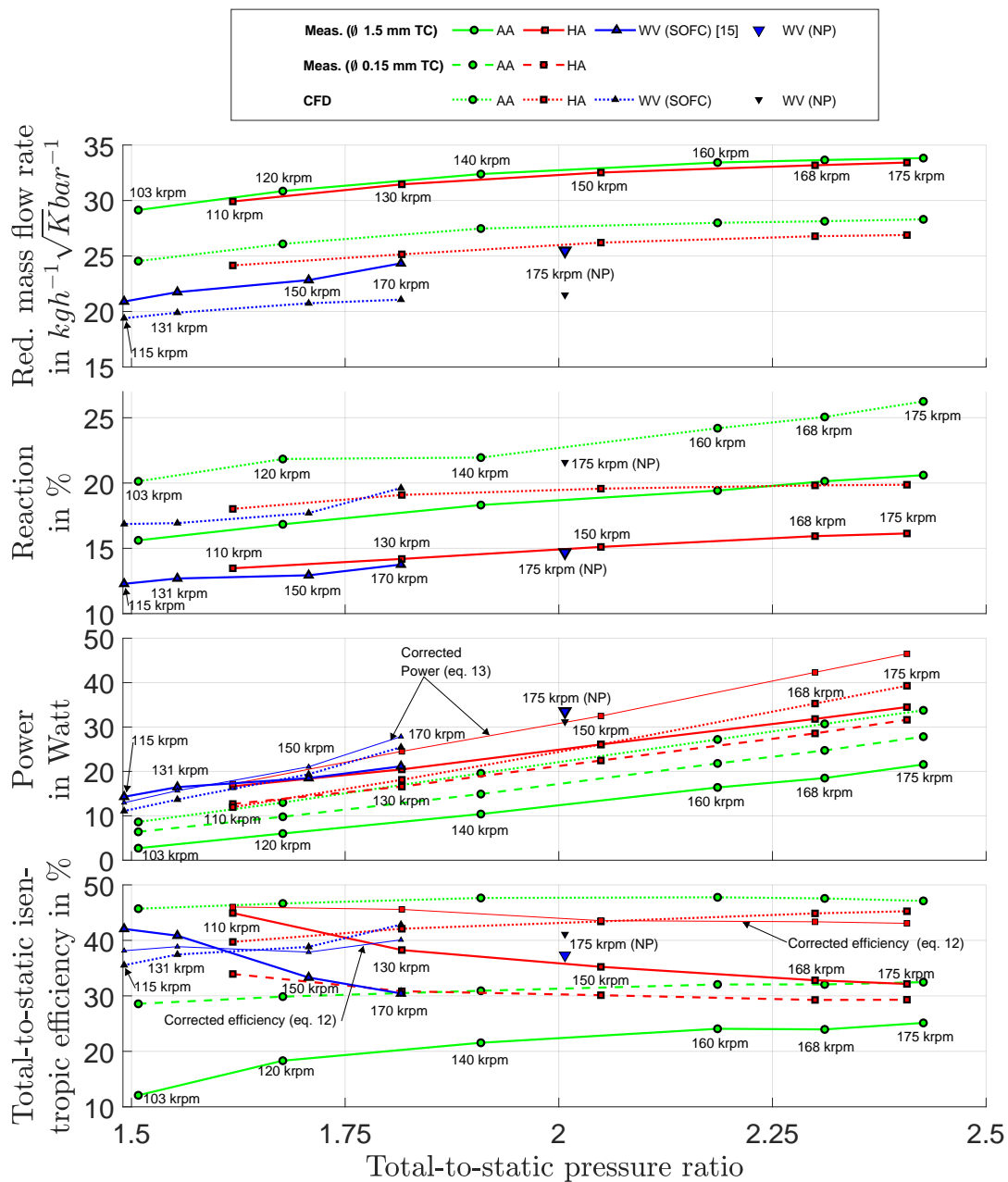
GTP-20-1474-FIGURE 3. (A) OPTICAL MICROSCOPY WITH HIROX KH-8700 OF THE TURBINE STATOR AND ROTOR (DIGITALLY MIRRORED) AND (B) OVERVIEW OF TURBINE STATOR (DOWNSIDE-UP) AND ROTOR WITH TURBINE INDUCER. THE CFD INLET BOUNDARY CONDITION (BC) AT SECTION 4 AND OUTLET BOUNDARY CONDITION AT SECTION 9 ARE MARKED IN (B) WITH DASHED LINES. THE STATOR AND ROTOR LEADING AND TRAILING EDGES (5, 6, 7, AND 8, RESPECTIVELY), ARE MARKED IN (A) WITH DASHED LINES.



GTP-20-1474-FIGURE 4. PIPING & INSTRUMENTATION DIAGRAM OF THE FAN-TURBINE UNIT TEST RIG SHOWING (A) A SCHEMATIC OVERVIEW OF THE AUXILIARY EQUIPMENT, (B) A TO-SCALE OVERVIEW OF THE MEASUREMENT SECTIONS OF THE TURBINE AND THE FAN INSIDE THE ELECTRICAL OVEN, (C) A ZOOMED MERIDIONAL VIEW OF THE STEAM TURBINE AND VOLUTE, (D) A ZOOMED SIDE VIEW OF THE FAN AND VOLUTE, AND (E) A PICTURE OF THE ACTUAL IMPLEMENTATION WITH GLASS FIBER INSULATION TAPES. THE TURBINE CAN BE EITHER DRIVEN WITH AIR (1) OR STEAM (2).



GTP-20-1474-FIGURE 5. DOMAIN REGIONS (RIGHT): INDUCER, STATOR, ROTATING TURBINE IMPELLER, AND EXDUCER DOMAIN FROM THE TOP TO THE BOTTOM, AND GENERATED MESH (LEFT) AT THE HUB FOR EACH DOMAIN FROM THE BOTTOM VIEW. THE FLUID-TO-FLUID INTERFACES ARE MARKED GREEN.



GTP-20-1474-FIGURE 7. THE TURBINE CHARACTERISTIC WITH AMBIENT AIR (AA, GREEN CIRCLES), HOT AIR (HA, RED SQUARES), AND WATER VAPOR (WV, BLUE TRIANGLES) FOR THE MEASUREMENT (MEAS.) WITH THE $\varnothing 1.5$ mm THERMOCOUPLES ACCORDING TO EQ. (6) AND (8) (SOLID LINES), THE $\varnothing 0.15$ mm THERMOCOUPLES ACCORDING TO EQ. (7) AND eq. (9) (DASHED LINES), AND THE STEADY SINGLE PASSAGE CFD SIMULATIONS (DOTTED LINES). THE TURBINE INLET TOTAL TEMPERATURES ARE 24 °C (AA), 218 °C TO 219 °C (HA), AND 211 °C (WV AT THE NOMINAL POINT). THE FOUR WATER VAPOR CASES (115 krpm, 131 krpm, 150 krpm, AND 170 krpm) ARE EXTRACTED FROM WAGER ET AL. [15] FOR THE OPERATION IN THE RELEVANT ENVIRONMENT WITH A 6 kW_e SOFC. THE AMBIENT PRESSURES RANGES FROM 0.96 bar TO 0.98 bar.

$s_{t,4}=f(T_{t,4},p_{t,4})$ and $h_{t,1}=h_{t,4}=f(T_{t,4},p_{t,4})$	
Estimations for first iteration: $\eta_{is,tst}=1$ and $\rho_8 \approx \rho_7$	
While $res > 1e^{-6}$	
Calculate rotor inlet velocity triangle ^a (\vec{u}_7 , \vec{c}_7 , and \vec{w}_7)	
Calculate rotor outlet velocity triangle ^a (\vec{u}_8 , \vec{c}_8 , and \vec{w}_8)	
$\Delta h_{is,tst}=f(\text{eq. 10})$	
$\Delta h_{tt}=\Delta h_{is,tst}\eta_{is,tst}$	
$h_{st,8}=h_{t,4}-\Delta h_{tt}-c_8^2/2$	
Static pressure: $p_{st,8} \approx p_{st,9}$	
Density $\rho_8=f(h_{st,8},p_{st,8})$ and dyn. viscosity $\nu_8=f(h_{st,8},p_{st,8})$	
Calculate new efficiency ($\eta_{is,tst,new}$) with	
Balje similarity concepts	Soderberg loss model
$\dot{V}_8=\dot{m}_1/\rho_8$	$\zeta=f(\text{eq. 17})$
$n_s=f(\text{eq. 4})$	$d_{hyd,8}=f(\text{eq. 20})$
$d_s=f(\text{eq. 16})$	$Re_{hyd,8}=c_8 d_{hyd,8} \rho_8 / \nu_8$
$\eta_{is,tst,new}=f(n_s,d_s)$ in 5.44 [18]	$\zeta_{stator}=f(\text{eq. 18})$
Correct for S/H in 5.31 [18]	$\zeta_{rotor}=f(\text{eq. 19})$
Correct for t/H in 5.32 [18]	$\eta_{is,tst,new}=f(\text{eq. 21})$
$res= \eta_{is,tst,new}-\eta_{is,tst} /\eta_{is,tst}$	
$\eta_{is,tst}=\eta_{is,tst,new}$	

^a The deviation at the stator and rotor TE is assumed to 0

GTP-20-1474-FIGURE 8. NASSI-SCHNEIDERMAN DIAGRAM OF THE EFFICIENCY CALCULATION WITH SIMILARITY CONCEPTS BY BALJE [17] AND LOSS CORRELATIONS BY SODERBERG [18].